crystals

MDPI

Review

The Effects of Nanostructure on the Hydrogen Sorption Properties of Magnesium-Based Metallic Compounds: A Review

Luca Pasquini

Department of Physics and Astronomy, University of Bologna, 40127 Bologna, Italy; luca.pasquini@unibo.it; Tel.: +39-051-209-5149

Received: 27 January 2018; Accepted: 21 February 2018; Published: 23 February 2018

Abstract: In this review, I examine the influence of nanoscale materials features on the hydrogen-metal interaction. The small system size, the abundance of surfaces/interfaces, and the spatial distribution of phases are the key factors to understand the hydrogen sorption properties of nanomaterials. In order to describe nanoscale-specific thermodynamic changes, I present a composition and atomic quantitative model applicable to every hydride-forming material, independently on its structure. The effects of surface free energy, interface free energy, and elastic constraint, are included in a general expression for the thermodynamical bias. In the frame of this model, I critically survey theoretical and experimental results hinting at possible changes of thermodynamic parameters, and in particular, enthalpy and entropy of hydride formation, in nanostructured Mg-based metallic compounds as compared to their coarse-grained bulk counterparts. I discuss the still open controversies, such as destabilization of ultra-small clusters and enthalpy–entropy compensation. I also highlight the frequently missed points in experiments and data interpretation, such as the importance of recording full hydrogen absorption and desorption isotherms and of measuring the hysteresis. Finally, I try to address the open questions that may inspire future research, with the ambition of tailoring the properties of hydride nanomaterials through a deeper understanding of their thermodynamics.

Keywords: nanostructures; hydrogen; magnesium; interfaces; thermodynamics; enthalpy; entropy; alloying; palladium; titanium

1. Introduction

Hydrides are a class of materials characterized by the presence of hydrogen (H) atoms bound with other elements in ionic (either negative H^- or protonic H^+ ions), covalent, or metallic (interstitial) forms [1]. These materials have originally gained considerable attention by virtue of their reversible hydrogen sorption properties, which fueled the worldwide effort to develop safe and efficient hydrogen storage media for mobile applications [2,3]. Hydride-forming metals are particularly fascinating because their atomic/electronic structure, and consequently many properties (thermal, optical, electrical, etc.), can be switched in parallel with the metal↔hydride transformation, i.e., by tuning the hydrogen pressure $p(H_2)$ and temperature conditions. This unique feature has been exploited in several applications, such as smart sensors and windows [4], hydrogen compressors without moving parts [5], heat storage systems [6], and cryogenic coolers [7]. Nickel-metal hydride batteries are the most successful commercial application of hydrides, powering 70% of the hybrid electric vehicles sold in 2014 [7]. Other exciting applications of hydrides in electrochemical energy storage are the use of complex borohydrides as solid electrolytes [8] and magnesium hydride conversion cathodes for lithium-ion batteries [9].

Magnesium (Mg) and its hydride (MgH_2) surely represent one of the most studied metal–hydrogen systems [10,11]. This is due to several attractive characteristics of Mg, namely the high

abundance (0.13 wt% in sea water and 2.76 wt% in the earth crust [12]), low cost, environmental compatibility, and of course lightness. MgH_2 has moderately high gravimetric and volumetric hydrogen density of ρ_m = 7.6 wt% H and ρ_V = 110 kg H/m^3. The formation of MgH_2 from Mg and H is an exothermic process with enthalpy $\Delta H^0 \cong -74$ kJ/mol H_2 and entropy $\Delta S^0 \cong -133$ J/K mol H_2 [13,14]. From the point of view of reversible hydrogen storage, these figures reveal that MgH_2 is far too stable to allow hydrogen desorption at $p(H_2)$ = 1 bar below 100 °C, as it would be necessary to feed a proton exchange membrane fuel cell [15]. In fact, using the van 't Hoff equation (see Section 2.1), it can easily be calculated that the decomposition temperature at $p(H_2)$ = 1 bar is about 283 °C. Conversely, the strongly negative formation enthalpy makes Mg and Mg-based compounds appealing for heat storage applications, e.g., in concentrated solar power plants [6,12]. MgH_2 is an insulator with a band gap of about 4.2 eV and therefore the metal–hydride transformation in Mg films induces a remarkable optical change from reflective to transparent. This behavior can be exploited to study H-sorption in thin films and nanostructures [16], where the sensitivity of bulk techniques based on pressure or mass changes would be insufficient.

The hydrogen sorption properties of a material can be modified in two ways. The more obvious is the change of its composition, typically playing with elements that have different bonding strengths with hydrogen. This approach may yield either solid solutions or compounds with a new crystalline structure, and has pushed the development of successful ternary hydrides such as $LaNi_5H_6$ and $FeTiH_2$ [17]. The other approach exploits the unique features of nanostructured materials and takes advantage of the continuous development in synthesis techniques and in high-resolution structural characterization methods [18].

Nanostructured materials, the building blocks of which are smaller than ≈100 nm in at least one spatial direction, constitute a bridge between the molecular world and bulk solids at the true thermodynamic limit. Their equilibrium and transport properties may depart significantly from those of bulk counterparts with the same chemical composition. The new physics and chemistry at the nanoscale stem essentially from two peculiar features, namely the small size and the high volume fraction occupied by surfaces/interfaces. These two fingerprints of all nanomaterials are intimately connected because the volume fraction of surfaces/interfaces scales inversely with the system size.

The "small size" condition is defined via a comparison to a characteristic length of the material, like for instance the mean free path of particles or excitations (electrons, phonons and magnons) that carry of energy, charge and spin. Alternatively, it could be the length of a magnetic interaction or the Bohr radius of a bound exciton. The spatial extensions of microstructural defects provide other examples of characteristic lengths, e.g., the width of magnetic domain walls, the width of antiphase boundaries, and the critical size of Frank–Read dislocation sources. New properties can be expected whenever the systems size L, in at least one spatial direction, is similar to or smaller than one of these *intrinsic* length scales. If such a condition applies, one speaks of a *confinement effect* on the material's properties. At the same time, the de Broglie wavelength λ_{dB} of the aforementioned carriers can be similar to L. By analogy with the quantized energy levels of plane waves confined in a box of width L, we can guess that the separation ΔE between two levels will scale inversely with some power of L. Therefore, with decreasing L, one enters a new world in which the condition $\Delta E > k_B T$ holds, meaning that adjacent energy levels are no longer mixed up by thermal excitations and that a *quantization effect* can emerge on properties, which are normally continuous in bulk materials. One of the most enlightening cases of confinement and quantization is the quantized electrical conductance at a quantum point contact of a 2-dimensional electron gas (2DEG) [19].

The abundance of interfacial regions in nanomaterials implies that the local environment of a macroscopically relevant fraction of constituent atoms differs significantly from the ideal crystalline structure. In fact, for atoms located at interfaces and surfaces, the number and the chemical species of neighboring atoms, as well as the bond lengths and bond angles, are not the same as for inner atoms. This structural difference brings about significant changes in many properties, often in opposite directions. For instance, at surfaces/interfaces the mass transport is faster than in the bulk due

to their less dense atomic packing [20], whereas the electrical conductivity drops due to scattering of charge carriers. The abundance of surface atoms with diverse local environment is particularly relevant in the field of heterogeneous catalysis, where both the activity and selectivity towards a given reaction product depend on very specific surface sites [21]. Surfaces/interfaces are characterized by an excess enthalpy due to missing or weakened interatomic bonds and by an excess entropy arising both from enhanced structural disorder and from soft modes in the vibrational density of states [22]. Enthalpy and entropy bring opposite contributions to the Gibbs free energy and therefore compete in the stabilization of the microstructure. However, the enthalpy term usually overwhelms the entropic one so that nanoscale materials are prone to coarsening phenomena when exposed to high homologous temperatures.

The spatial distribution of elements within a multi-component nanoscale object offers a new degree of freedom for its thermodynamic description. The classical distinction between random mixing, short-range-order and clustering, so successful in bulk binary alloys, must be extended to encompass various spatial arrangements in the case of *nanoalloys*. As an example, different clustering patterns in a binary NP may result in various morphologies such as Janus-like, surface-segregated or onion-like structures [23]. The interplay between these variants enriches the corresponding phase diagram by mapping new temperature–composition regions where one specific morphology is the most stable.

This review is organized as follows: in Section 2, I address the influence of system size, abundance of surfaces/interfaces, and spatial distribution of phases, on the hydrogen sorption properties of nanoscale materials. I specifically discuss the effects of surfaces, interfaces, elastic constraint and alloying. I present a quantitative model to predict and explain thermodynamic changes and discuss general ideas applicable to every hydride-forming material, independently on its composition and atomic structure. In Section 3, I critically examine selected experimental results on Mg-based nanostructures, starting with pure Mg in Section 3.1 and moving to Mg alloys and compounds in Sections 3.2–3.5. In the Conclusions, I summarize the major findings and share some ideas for future research directions. I note that excellent reviews both on size effects [24,25] and on the synthesis of nanostructured Mg-based hydrides [11,26] have been published. The peculiarity of the present work is the critical comparison between theory/modeling and experimental results. I put great care in assessing the reliability of the thermodynamic parameters extracted from the analysis of experimental data. After about 20 years of intense worldwide research on nanostructured hydrides, often characterized by sensational claims and contrasting reports, I hope to clarify some still open controversies, to draw the reader's attention to frequently missed points in the interpretation of hydrogen sorption data, and to stimulate future research activities.

2. Hydrogen in Nanostructured Alloys and Compounds

In order to characterize the interaction of hydrogen with nanomaterials, a thorough description of both thermodynamics and kinetics of hydrogen sorption is required. The following sub-sections will separately treat nanoscale effects on thermodynamics and kinetics.

2.1. Nanoscale Effects on Thermodynamics

Thermodynamics essentially deals with the equilibrium behavior represented in a phase diagram and dependent on fundamental parameters such as the enthalpy and entropy of hydrogen solution in the host material and the enthalpy and entropy of hydride formation. Hydrogen solution in the metallic phase (usually denoted as α-phase) takes place up to a limiting composition MH_{x_α}, where the symbol M stands generically for the metallic element(s) and H for hydrogen. Above this limit,

the hydride phase (usually called β-phase) starts to develop in coexistence with the α-phase until the composition MH_{x_β} is attained, at which the α-phase disappears. The corresponding reaction is:

$$MH_{x_\alpha} + \frac{x_\beta - x_\alpha}{2} H_2 \rightarrow MH_{x_\beta}. \quad (1)$$

The knowledge of thermodynamic parameters makes it possible to predict the concentration of hydrogen in the α-phase as a function of pressure and temperature and the temperature dependence of the *plateau pressure* where the α- and β-phases coexist in equilibrium. The plateau pressure of (1), for a bulk system, is given by the van 't Hoff equation:

$$\ln\left(\frac{p_{eq,bulk}}{p_0}\right) = \frac{2\Delta g^0_{bulk}}{RT(x_\beta - x_\alpha)} = \frac{\Delta G^0_{bulk}}{RT} = \frac{\Delta H^0_{bulk}}{RT} - \frac{\Delta S^0_{bulk}}{R}, \quad (2)$$

where $p_{eq,bulk}$ is the pressure of hydrogen gas in equilibrium with the α- and β-phases at temperature T and R is the gas constant. Here Δg^0_{bulk} represents the Gibbs free energy of reaction (1) at standard conditions (pressure p_0), and ΔG^0_{bulk} is the same quantity per mole H_2. ΔH^0_{bulk} and ΔS^0_{bulk} are the enthalpy and entropy per mole H_2.

Nanoscale effects may bring about a *thermodynamical bias*, i.e., a change of the reaction free energy with respect to the bulk:

$$\delta\Delta G^0 \equiv \Delta G^0{}_{nano} - \Delta G^0_{bulk}. \quad (3)$$

Such a bias reflects into a shift of the equilibrium pressure, according to:

$$\ln\left(\frac{p_{eq,nano}}{p_{eq,bulk}}\right) = \frac{\delta\Delta G^0}{RT}. \quad (4)$$

I will now discuss the four main clues to induce a thermodynamical bias through the exploitation of nanoscale-specific features.

2.1.1. Surface Free Energy

The high surface area typical of nanoparticles (NPs), nanowires and uncapped thin films modifies the thermodynamics of hydride formation if the surface free energy of the metal differs from the hydride. The surface free energy is given by the surface area A multiplied by the specific energy per unit area, γ. Usually the surface area is larger in the higher-volume hydride phase, an exception being thin films that expand perpendicularly to the substrate plane. The thermodynamical bias is given by a summation over all surface elements according to:

$$\left(\delta\Delta G^0\right)^{sur} = \frac{2\overline{V}_M}{(x_\beta - x_\alpha)V_{nano}}\left(\sum_{i,sur}\{A\gamma\}_{MH_{x_\beta}|i} - \sum_{i,sur}\{A\gamma\}_{MH_{x_\alpha}|i}\right). \quad (5)$$

where $\overline{V}_M$ is the molar volume of M and V_{nano} is the volume of the nano-system in the α-phase. The subscripts '$MH_{x_\beta}|i$' and '$MH_{x_\alpha}|i$' denote the i-th surface element in the β- and α-phase, respectively. Equation (5) includes two separate summations because the equilibrium crystal shape of the nano-system in the β-phase can be different from that in the α-phase. Using density functional theory (DFT) and the Wulff construction, Sholl and co-workers have calculated the enthalpic contribution $(\delta\Delta H^0)^{sur}$ to Equation (5) as a function of the NP radius for several metals [27]. Their results are reproduced in Figure 1a. They also found that the enthalpy change normalized to the NP's surface area correlates with the value of the charge on the H atom for the metals Na, Mg, Al, Sc, Ti, and V, whereas Li deviates significantly from this trend. For Mg and Na, $(\delta\Delta H^0)^{sur}$ is positive, meaning that the hydride is less stable due to surface effects, whereas the opposite occurs for Li, Al, Sc, Ti and V. For much smaller NPs composed of few metal atoms, DFT calculations from

different authors show significant discrepancies. Wagemans et al. calculated a strong destabilization of the hydride starting below 19 Mg atoms [28], as shown in Figure 1b. Differently, Shevlin and Guo calculated that $(MgH_2)_n$ nanoclusters with $4 < n < 11$ are more stable than the bulk [29], pointing out the necessity to determine the true minimum energy structure. Using data mining techniques, they showed the presence of H atoms with 1–3-fold coordination and Mg atoms with 4–7-fold coordination in the $(MgH_2)_n$ nanoclusters. These minimum energy cluster structures therefore depart significantly from the bulk, where H and Mg are 3-fold and 6-fold coordinated, respectively. An example of this stabilizing reconstruction is given in Figure 1b for the cluster with $n = 6$ [29]. Quantum Monte Carlo simulations by Wu et al. provided a picture similar to Shevlin and Guo, suggesting that clusters with $6 \leq n < 20$ are stabilized compared to the bulk while a strong destabilization starts at $n = 4$ [30].

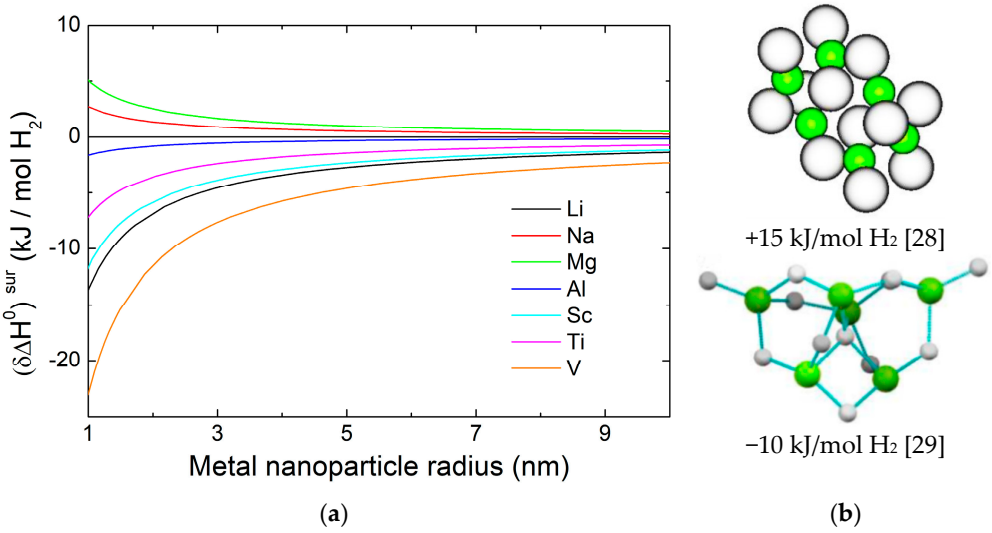

Figure 1. (**a**) Variation of the hydride formation enthalpy as a function of the nanoparticle (NP) radius (>1 nm) relative to the respective bulk materials. The curves are drawn using the parameters calculated in [27]. As a reference, remind that a NP with $r = 1$ nm contains about 200 Mg atoms; (**b**) Atomic structures of $(MgH_2)_6$ clusters and corresponding $(\delta\Delta H^0)^{sur}$ values calculated by DFT, taken from Refs. [28] (top, B97 functional) and [29] (bottom, LDA functional), showing strong discrepancies among different authors. The green spheres represent Mg and the white spheres H. In both (**a**) and (**b**), positive $(\delta\Delta H^0)^{sur}$ values imply that the nano-hydride is less stable than the bulk hydride.

In summary, surface effects give rise to an enthalpy shift $(\delta\Delta H^0)^{sur}$ that can be negative or positive depending on the material under consideration. For MgH_2, the calculations in [27] predict a destabilization of about 5 kJ/mol H_2 in NPs with a radius of about 1 nm. The comparison between theory and experiments will be discussed in Section 3.1.1. For smaller $(MgH_2)_n$ NPs composed of few metal atoms ($n < 20$), contrasting calculations were reported in the literature [28–30]. Clearly, the preparation, stabilization against sintering, and oxidation resistance of ultra-small MgH_2 nanoclusters pose tantalizing challenges. Up to now, experiments have not assessed whether a stabilization or a destabilization of the hydride takes place in this extreme nanosize regime.

2.1.2. Interface Free Energy

In the previous section, I dealt with surfaces, i.e., specific solid–vapor interfaces. Equation (5) can be generalized to include all interfaces, in particular the solid–solid interfaces, which are ubiquitous in nanoscale materials. The general expression for the thermodynamical bias becomes:

$$\left(\delta\Delta G^0\right)^{int} = \frac{2\overline{V}_M}{\left(x_\beta - x_\alpha\right)V_{nano}}\left(\sum_{i,int}\{A\gamma\}_{MH_{x_\beta}|i} - \sum_{i,int}\{A\gamma\}_{MH_{x_\alpha}|i}\right), \quad (6)$$

where the summations now extend over all interfaces, including also surfaces as solid–vapor interfaces.

From the theory/modeling point of view, the problem rests in the determination of the relaxed interfacial structure and in the calculation of its thermodynamic parameters. This has been done for model metal–hydride and hydride–hydride interfaces with well-defined crystallographic orientation and coherent structure [31,32]. Figure 2 depicts the case of specific Mg/TiH_2 and MgH_2/TiH_2 interfaces [32], which are relevant for the hydrogen sorption properties of Mg/TiH_2 layered films and nanocomposites. In real systems, particularly in ball-milled materials, many different types of interfaces may be present.

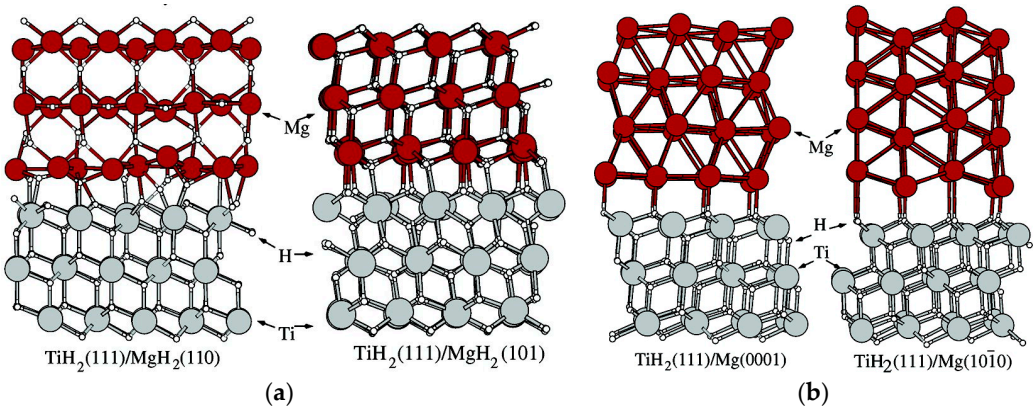

Figure 2. (**a**) Interface structure of $TiH_2(111)/MgH_2(110)$ and $TiH_2(111)/MgH_2(101)$; (**b**) Interface structure of $TiH_2(111)/Mg(0001)$ and $TiH_2(111)/Mg(10–10)$. Reprinted with permission from [32]. Copyright 2012 American Chemical Society.

Equation (6) can be simplified if the number of interfaces does not change upon hydride formation/decomposition, as in a sandwiched thin film. In this case, one can use only one summation:

$$\left(\delta\Delta G^0\right)^{int} = \frac{2\overline{V}_M}{\left(x_\beta - x_\alpha\right)V_{nano}} \sum_{i,int} \left(\{A\gamma\}_{MH_{x_\beta}|i} - \{A\gamma\}_{MH_{x_\alpha}|i} \right). \quad (7)$$

Moreover, it may also happen that the areas of the relevant interfaces undergo negligible changes. As an example, let us consider again a sandwiched thin film: if the clamping to the adjacent layers is strong enough, the volume change that accompanies hydride formation/decomposition takes place only through a change of the film thickness. The metal and the hydride then have the same interface areas A_i with the surrounding layers. Since the small lateral interfaces give a negligible contribution to the thermodynamical bias, it is possible to rewrite:

$$\left(\delta\Delta G^0\right)^{int} = \frac{2\overline{V}_M}{\left(x_\beta - x_\alpha\right)V_{nano}} \sum_{i,int} A_i \Delta\gamma_i, \quad (8)$$

where $\Delta\gamma_i \equiv \gamma_{MH_{x_\beta}|i} - \gamma_{MH_{x_\alpha}|i}$ is the specific free energy difference between hydride and metal for the i-th interface. Equation (8) can be applied also to a hydride-forming particle with embedded inclusions that do not react with hydrogen. Finally, if it can be assumed that $\Delta\gamma_i = \Delta\gamma \; \forall \; i$, i.e., that all interfaces are equivalent as far as the specific free energy difference is concerned, the thermodynamical bias takes the simple form:

$$\left(\delta\Delta G^0\right)^{int} = \frac{2\overline{V}_M}{\left(x_\beta - x_\alpha\right)} \frac{A_{nano}}{V_{nano}} \Delta\gamma, \quad (9)$$

in which the first fraction is proportional to the metal molar volume (the proportionality constant being 1 for the Mg–MgH_2 system), and the second fraction is a geometrical factor given by the ratio of the total area A_{nano} to the volume V_{nano} of the nano-object. For a film of thickness d this factor equals $2/d$.

Similar to the bulk free energy, the $\Delta\gamma_i$ include enthalpy and entropy contributions:

$$\Delta\gamma_i = \Delta h_i - T\Delta\sigma_i \Rightarrow \Delta\gamma = \Delta h - T\Delta\sigma \text{ if } \Delta\gamma_i = \Delta\gamma \; \forall \; i. \tag{10}$$

Under the applicability conditions of Equation (9), one can see that the thermodynamical bias vanishes at a compensation temperature T_{comp}, which does not depend on the geometrical factor A_{nano}/V_{nano} and is given by:

$$T_{comp} = \Delta h/\Delta\sigma. \tag{11}$$

where Δh and $\Delta\sigma$ are the specific interface enthalpy and entropy difference, which are assumed to be the same for all relevant interfaces. The remarkable implication of Equation (11) is that thin films having the same type of interfaces should display an equilibrium pressure equal to the bulk at the temperature T_{comp}, independently on their thickness.

The calculations that appeared so far in the literature dealt only with the surface/interface free enthalpy. I am not aware of modeling studies that were able to determine the surface/interface entropy contribution to the thermodynamical bias in nanomaterials. However, this may be an important correction to the enthalpy term. A tendency towards stabilization of the hydride is expected if the vibrational plus configurational surface/interface entropy of the β-phase is larger than that of the α-phase. Future theoretical activity in this field is needed in order to tailor the thermodynamic properties of nanoscale hydrides through rationally designed interfaces.

2.1.3. Elastic Constraints

Another possible source of thermodynamical bias emerges in mechanically confined nanomaterials when the surrounding phases constrain the volume change that accompanies the $\alpha \leftrightarrow \beta$ phase transformation. The situation is depicted in Figure 3a for a hydride-forming NP clamped by a non-reacting, elastically stiff shell. In this situation, the hydride phase experiences a compressive (negative) volume strain ε_V^β and is therefore destabilized. The bias on the hydride formation enthalpy is given by [33]:

$$\left(\delta\Delta\mathrm{H}^0\right)^{el} = -2B\overline{V}_H\varepsilon_V^\beta, \tag{12}$$

where B is the bulk modulus of M and $\overline{V}_H$ the partial molar volume of hydrogen in the β-phase.

Similarly, one could consider a clamped hydride NP that is not free to contract when hydrogen is released. This type of constraint produces a tensile (positive) strain in the α-phase, making the metal less stable and increasing the absolute value of the reaction free energy. The calculation of $\left(\delta\Delta\mathrm{H}^0\right)^{el}$ is essentially an elasticity problem. Analytical solutions were provided for clamped thin films [34] and for core-shell spherical NPs [33], and approximate results were derived for cylindrical nanodots [35]. The appeal of this approach, sometimes called elastic strain engineering, lies in the potential ability to tune the thermodynamics significantly even with experimentally manageable NPs sizes. This is shown in Figure 3b where an enthalpy change of about 14 kJ/mol H_2 for an Mg-MgO core-shell NPs of 25 nm radius and 3 nm shell thickness is predicted [33]. This destabilization would outperform the one achievable through surface free energy effects in much smaller Mg NPs of 1 nm radius [27]. The main problem that hampers its practical implementation is that the elastic stresses easily exceed the mechanical yield strength of the material, resulting in the onset of plastic deformation and in a drastic drop of the elastic strain. The comparison with experimental data will be discussed in Section 3.1.3.

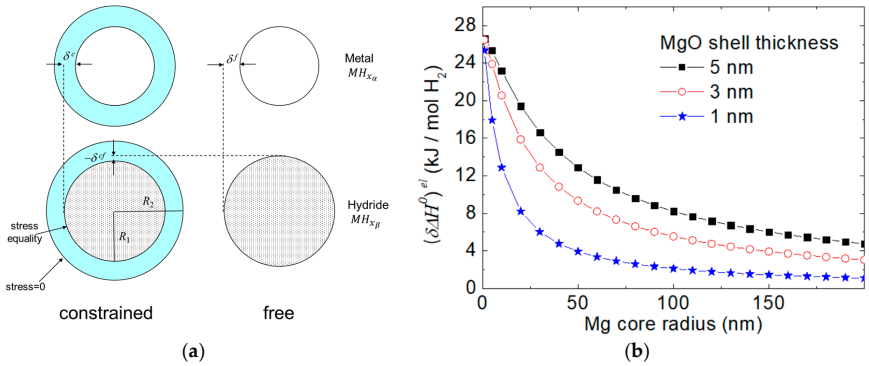

Figure 3. (**a**) Schematic representation of the elastic constraint mechanism in a hydride-forming NP embedded in a spherical shell; (**b**) hydride destabilization calculated for a Mg-MgO core-shell NP as a function of the radius, for three different thickness of the MgO shell [33].

2.1.4. Alloying Effects

Alloying is a widely explored strategy to tune the thermodynamics of a multicomponent hydride system. In principle, this approach is not restricted to nanomaterials; however, since alloying is often obtained through ball milling, a nanoscale microstructure develops.

Let us consider a single hydride-forming element M, that undergoes reaction (1) (with $x_\alpha \approx 0$ for the sake of simplicity), and introduce a second element N that forms an alloy MN_y in the metallic state. Upon hydrogen absorption, different scenarios are possible depending on the hydride formation enthalpy of N and on y. The two extreme variants of reaction (1) are:

$$MN_y + \frac{x_\beta}{2}H_2 \rightarrow MH_{x_\beta} + yN, \tag{13}$$

in which the hydride has the same composition as for the pure M element and N is segregated, and:

$$MN_y + \frac{x_\beta}{2}H_2 \rightarrow MN_yH_{x_\beta}, \tag{14}$$

in which only the β-phase is obtained with preservation of the MN_y stoichiometry. The actual value of x_β needs not be the same in the two cases. Other schemes are clearly possible, like disproportionation reactions that involve intermediate alloy compositions.

A further possibility is that M and N are immiscible in the metal but form a ternary hydride:

$$M + yN + \frac{x_\beta}{2}H_2 \rightarrow MN_yH_{x_\beta}\,. \tag{15}$$

The idea behind reaction (14) has led to the successful development of ternary hydrides such as $LaNi_5H_6$, $FeTiH_2$, Mg_2NiH_4, based on the alloying of elements with strongly different heats of hydride formation [17]. For low y values, the element N in (14) can be seen as a dopant within the M matrix. The effects of dopants on thermodynamics has been investigated theoretically with particular focus on transition metals (TMs) in MgH_2 [36–38]. Paskaš Mamula et al. have calculated the excess charge on the entire 3d TM series of dopants in MgH_2 (Figure 4a) and have found a correlation with the desorption enthalpy [38]: the higher the electronic charge transfer from the H ion to the TM dopant, the less stable the hydride. The largest hydride destabilization was predicted for Fe, Co, Ni, in qualitative agreement with calculations of Shevlin and Guo [29] of Ni-doped $(MgH_2)_n$ clusters (Figure 4b).

As shown in Figure 5, the difference between the enthalpies of reactions (13) and (1) is given by the enthalpy of alloy formation $(\delta\Delta H^0)^{al}$. The reader interested in thermodynamic tuning of hydride formation in Mg alloys is referred to a comprehensive recent review [12]. I just remark here two features that are relevant in nanomaterials:

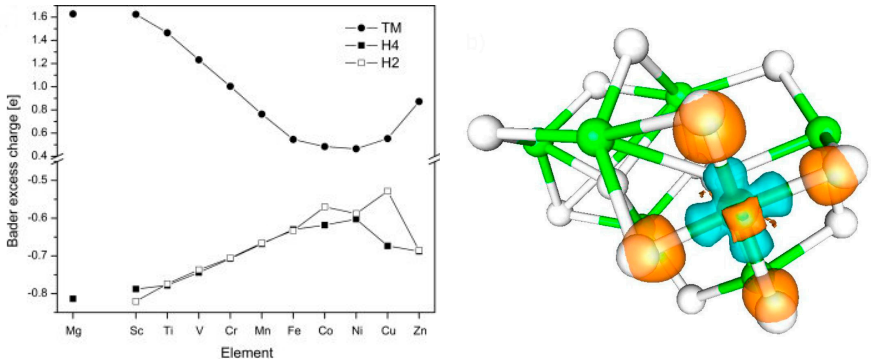

Figure 4. (**a**) Bader excess charge on transition metal (TM) dopants and on nearest neighbor H atoms for the entire MgH_2:TM 3d series (the value for pure MgH_2 is shown on the left). Reprinted with permission from Ref. [38]. Copyright 2014 Hydrogen Energy Publications, LLC; (**b**) Charge density difference of Ni-doped $(MgH_2)_7$ cluster, orange denoting charge density depletion and blue accumulation. In agreement with (**a**), electronic charge is transferred from H^- ion to d-state of the Ni dopant. Reprinted with permission from [29]. Copyright 2013 American Chemical Society.

1. Nanoscale dispersion of phases is required to keep the solid-state diffusion lengths short, thus making it possible kinetic reversibility of reactions (13) and (15).
2. In nanoalloys, the phase separation that appears on the right of (13) or on the left of (15) may be realized through specific morphologies such as core-shell, core-satellite, or Janus, with shifted free energy with respect to bulk alloys (Figure 5). This potential route to thermodynamic tuning, which requires advances in the calculations of nanoalloys phase diagrams, is to our knowledge yet unexplored.

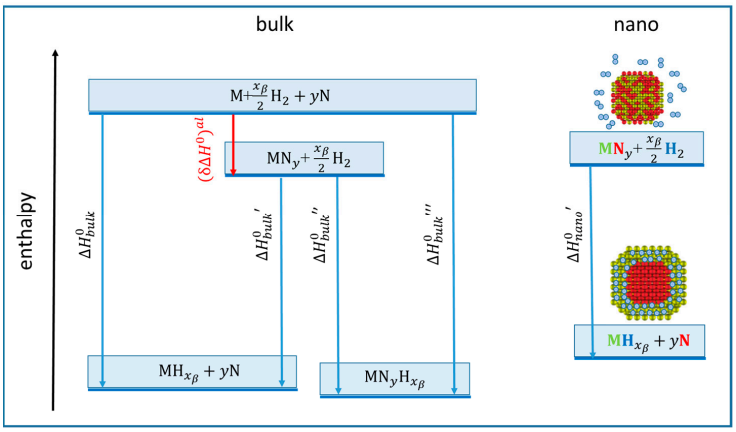

Figure 5. Schematic representation of thermodynamic tuning of reaction (1) (enthalpy ΔH^0_{bulk}) by addition of an element N that can: (i) form an alloy in the α-phase (reaction (13), enthalpy $\Delta H^0_{bulk}{}'$); (ii) form an alloy in the α-phase and a ternary hydride (reaction (14), enthalpy $\Delta H^0_{bulk}{}''$), or (iii) form a ternary hydride (reaction (15), enthalpy $\Delta H^0_{bulk}{}'''$). The enthalpy of reaction (13) in nanomaterials can be further tuned by different elemental distributions in the α- and β-phases. The example on the right shows the case of a metallic random alloy NP that transforms into a metal-metal hydride core-shell structure upon hydrogen absorption.

2.2. Nanoscale Effects on Kinetics

Kinetics aims at identifying the microscopic mechanisms of hydride formation and decomposition and at determining the activation energies of the rate-limiting step(s). The elementary steps involved in the metal-hydride transformation can be classified into:

- H_2 dissociation/recombination at the surface
- Penetration of atomic H in subsurface layers
- H diffusion in the α-phase (usually fast) and in the β-phase (typically fast in interstitial hydrides, but slow in ionic and covalent hydrides)
- Possible nucleation of the new phase (e.g., β within α or vice versa)
- Motion of the α/β interface

Each step is strongly dependent on the microstructure and on the presence of additives, such as catalytic phases that lower the activation energy for H_2 dissociation/recombination at the surface. The mechanisms and rate of the transformation are studied by monitoring a suitable signal, such as pressure, gas flow, heat flow or weight change, after a sudden transition out of equilibrium, typically induced by a fast pressure change or a rapid temperature scan. In a nanostructured material, several microstructural features concur to enhance the kinetics of hydrogen sorption:

1. Hydrogen has to diffuse over a length similar to the system size to complete the transformation. Since the diffusion time is proportional to the square of the diffusion length, a size reduction by three orders of magnitude (i.e., from ≈50 μm down to ≈50 nm) implies a shortening of the diffusion time by six orders of magnitudes. This is particularly relevant for the non-interstitial hydrides, in which hydrogen diffusion is typically slow.
2. The interfaces are short-circuit diffusion paths that further speed up hydrogen transport in and out of the material compared to hydrogen diffusion in the crystal. This argument applies both to homophasic interfaces such as grain boundaries in a nanocrystalline material and to heterophasic interfaces that are present in nanocomposites.
3. The surfaces/interfaces can be preferential sites for heterogeneous nucleation of the new phase.
4. If the surface of the host material is catalytically active, the rate of H_2 dissociation/recombination is proportional to the specific surface area. If the surface is poorly active, as for pure Mg, suitable catalytic additives must be dispersed at the nanoscale using techniques such as ball milling, wet chemistry, and vapor deposition [11,26].

3. Results and Discussion

The aim of this section is to survey quantitative experimental studies of hydrogen sorption in Mg-based nanomaterials and to compare them with the expectations based on the previously discussed arguments. Our main interest is directed towards thin films and NPs in various forms, i.e., freestanding, supported on microporous scaffolds and embedded in a matrix. The reason is that in these systems, the size is refined down to the nanometer scale in one spatial dimension at least. Differently, in ball-milled materials, the crystallite size may well be ~10 nm, but the powder particles are in the micrometer range. This microstructure can hardly induce any thermodynamical bias, although it can greatly improve the kinetics if suitable catalyst phases are added in the milling pot. The reader interested in kinetics of ball-milled MgH_2 with catalytic additives is referred to a recent comprehensive review [11].

I will examine in Section 3.1 the cases where the simple reaction (1) holds with M=Mg, and in Sections 3.2–3.5 the situations in which other elements or phases intervene according to schemes (13)–(15) or intermediate ones.

3.1. The $Mg+H_2 \leftrightarrow MgH_2$ Transformation at the Nanoscale

Figure 6 displays experimental thermodynamic data for the simple reaction $Mg+H_2 \leftrightarrow MgH_2$ in various classes of nanoscale materials (appropriate references are given in the caption). The data are grouped using different colors: red for freestanding NPs, blue for thin films and multilayers, green for supported or embedded NPs, and black for bulk and ball-milled Mg. Since alloying effects do not play a role here, the only possible sources of thermodynamical bias are the surface/interface free energy and the elastic strains. One can immediately notice that, despite the appearance of significantly reduced enthalpies, the equilibrium temperature at $p(H_2)$ = 1 bar is always quite close to the bulk value of 283 °C. Significant

departures from the bulk van 't Hoff plot are observed only for ultrathin films at low temperature around 100 °C. I will now discuss separately the nanomaterials classes that appear in Figure 6.

3.1.1. Nanoparticles (Freestanding)

The synthesis and hydrogen sorption properties of freestanding Mg NPs has been reported by several authors [39–43]. Probably due to the strong sintering of Mg with high surface area, the average NP diameter obtained in these studies was always above 10 nm. Many studies dealt mainly with kinetic properties at relatively high temperature >250 °C, and only few experiments were able to provide equilibrium data and to determine enthalpy/entropy values. Liu et al. synthesized Mg NPs by electroless reduction [43]: They observed that the absolute values of both enthalpy and entropy decrease with decreasing NP diameter below 50 nm, reaching 63.5 kJ/mol H_2 and 118.4 J/(K mol H_2) for a diameter of 15 nm [43]. These values are not compatible with theoretical calculations in this size range, where a small thermodynamic bias $(\delta\Delta H^0)^{sur} \approx 0.6$ kJ mol H_2 was predicted (see Section 2.1 and Refs. [27,28]). In fact, the equilibrium pressure–temperature data of Liu et al. were very close to the bulk van 't Hoff plot, a result that the authors attributed to enthalpy–entropy compensation. A specific reason for the enthalpy–entropy decrease was not proposed, but a possible different interaction of H with Mg at the nanoscale was speculated [43], suggesting that the calculations should be revised. In order to solve this controversy, the experiments should provide equilibrium data on a wider temperature span. Liu et al. determined their enthalpy/entropy values from the best linear fit of three (p,T) points in the 300–350 °C range. As shown very clearly by Cornish-Bowden [44], phantom correlations between slope (i.e., enthalpy) and intercept (i.e., entropy) of a van 't Hoff plot may appear due the narrow temperature range explored. It is therefore necessary to measure equilibrium data at significantly lower temperature, to better detect the presence of an enthalpic destabilization and to avoid issues arising from microstructural instabilities of Mg NPs at high temperatures.

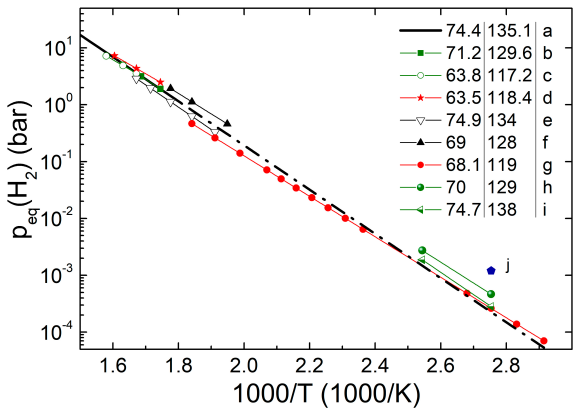

Figure 6. Compilation of van 't Hoff plots calculated from ΔH^0 and ΔS^0 data for Mg-based nanomaterials confronted to bulk Mg (curve **a** from Ref. [13]). The black dash-dotted line is the low temperature extrapolation of bulk Mg data. In the legend, the numbers in the columns denote the corresponding absolute values of ΔH^0 (left, in kJ/mol H_2) and ΔS^0 (right, in J/K mol H_2). The meaning of the colors is as follows: red for freestanding NPs; green for embedded or supported NPs; blue for thin films; black for ball-milled materials. The number of symbols represents the number of experimental points measured by the authors to determine enthalpy and entropy. **b**: 2–7 nm Mg nanocrystallites in LiCl matrix [14]. **c**: <3 nm Mg NPs in carbon scaffold [45]. **d**: 15 nm Mg NPs by electroless reduction [43]. **e**: MgH_2-TiH_2 ball-milled nanocomposite (30 at.% Ti) [46]. **f**: MgH_2-0.1TiH_2 ball-milled nanocomposite [47]. **g**: MgH_2-TiH_2 composite NPs, 10–20 nm in diameter (6–30 at.% Ti) [48]. **h**: Mg/Ti/Pd nanodots on silica, diameter 60 nm, and **i**: Mg/Ti/Pd nanodots on silica, diameter 320 nm [35]. **j**: ultra-thin (2 nm) Mg film sandwiched between TiH_2 layers [49].

Recently, we succeeded in characterizing both kinetics and thermodynamics of MgH_2-TiH_2 composite NPs down to 70 °C [48]. This remarkable achievement was made possible by the integration of gas-phase condensation synthesis of NPs and Sievert-type apparatus in a single ultra-high vacuum compatible system. NPs with diameter in the 10–20 nm range were measured in situ under very clean conditions, thus keeping surface contaminations by oxides/hydroxides as low as possible and achieving record-breaking low-temperature kinetics. At low temperatures in the range 70–100 °C, the equilibrium pressure was only slightly above the extrapolated van 't Hoff plot of bulk Mg (see Figure 6). In these composite NPs, the major source of thermodynamical bias arises from the high volume fraction of MgH_2/TiH_2 interfaces. The experimental enthalpy bias $(\delta\Delta H^0)^{int} \approx 6$ kJ/mol H_2 was in reasonable agreement with the predictions of Equations (9) and (10) assuming an average $\Delta h = 0.64$ J/m^2 as calculated in Ref. [32]. However, the entropy bias $(\delta\Delta S^0)^{int} \approx 16$ J/(K mol H_2) was about two times larger than calculated using $\Delta\sigma = 0.9 \times 10^{-3}$ J/K m^2, a value that corresponds to an interface entropy difference of 1 k_B per H atom between α- and β-phase [50].

3.1.2. Thin Films

Mg layers with a precisely controlled thickness down to a few nm represent an ideal playground to test the concept of thermodynamic tuning. It is important that the adjacent layers do not form alloys with Mg to single out genuine effects of interfaces and/or clamping. Baldi et al. showed that a Mg/MgH_2 layer sandwiched between two TiH_2 layers behaves as a quasi-free film [51]. This combination benefits from the mutual immiscibility of Mg and Ti; moreover, TiH_2 is permeable to hydrogen. A Pd capping layer is usually added to protect from oxidation and to facilitate H_2 dissociation/recombination at low temperatures.

The thermodynamics of ultra-thin Mg films was studied by measuring the optical transmission as a function of $p(H_2)$ under isothermal conditions. Figure 7a shows a series of isotherms at 90 °C for different thicknesses d of the Mg layer (a wedge-shaped film was actually employed in order to collect all the data in parallel). The upward shift of both absorption and desorption branches with decreasing d conveys a clear proof of destabilization. In fact, a ~5-fold increase of the equilibrium pressure compared to the extrapolation of bulk Mg data was recorded at 90 °C (see Figure 6). Figure 7b shows that the equilibrium pressure, and hence the thermodynamical bias, depends linearly on d^{-1}. This dependence is in accordance with the model Equation (9): The slope obtained from the linear fit yielded $\Delta\gamma = 0.33$ J/m^2, in qualitative agreement with but lower than the enthalpic values $\Delta h = 0.64$ J/m^2 calculated by DFT [49]. The difference may be due to the entropic contribution $-T\,\Delta\sigma$ that was not discussed by the authors despite the availability of $\Delta\gamma$ data at several temperatures in the 90–200 °C range.

Pivak et al. carried out a comprehensive study on Mg/M/Pd (M = Ti, Ta, Fe) films and determined enthalpy–entropy values for absorption and desorption separately [52]. They also developed a model to explain the hysteresis, as quantified by the ratio between the plateau pressures of absorption and desorption, in terms of elastic + plastic work during hydrogen loading and unloading [52].

Kalisvaart et al. extended the interface destabilization concept to Mg/AlTi multilayers with various $d/2$ configurations, where $2 \leq d \leq 10$ and 2 are the thicknesses in nm of Mg and AlTi layers, respectively [53]. In particular, the 2/2 multilayers showed a 20-fold increase of the absorption plateau pressure compared to bulk Mg at 200 °C. The value of $\Delta\gamma = 0.81$ J/m^2 obtained from absorption data was significantly higher than in Mg/TiH_2 multilayers. However, the desorption plateau pressures showed only a small increase above the bulk value. In other terms, the Mg/AlTi multilayers were affected by a large hysteresis, which in combination with the thermodynamical bias results in different shifts of absorption and desorption plateaus. As a consequence, no appreciable destabilization of the hydride was achieved.

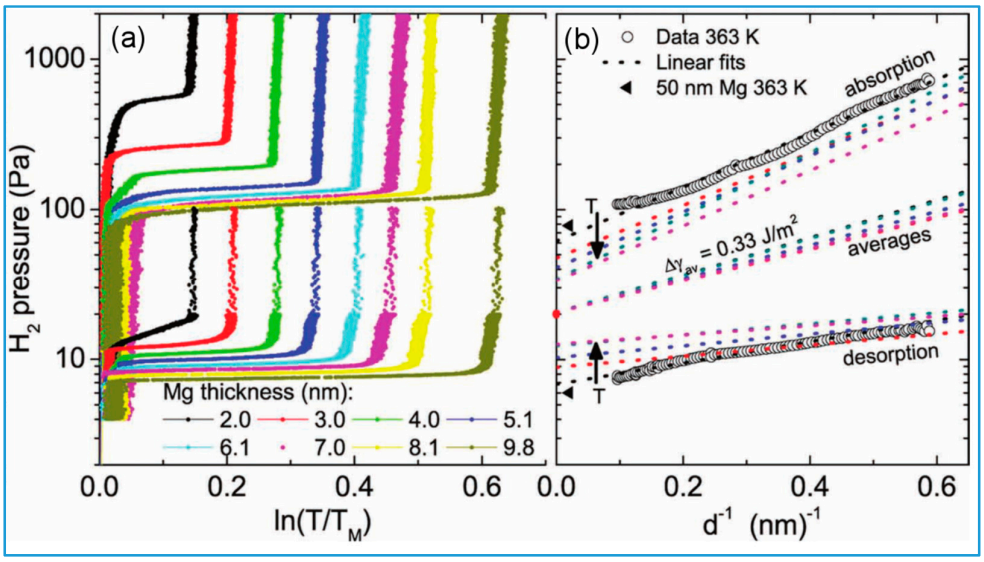

Figure 7. (**a**) Pressure-optical transmission isotherms at 90 °C as a function of the thickness d in a wedge-shaped Mg thin film sandwiched between TiH_2 layers; (**b**) Plateau pressures for absorption and desorption vs. d^{-1} at different temperatures in the range 363–473 K. The specific interface free energy can be calculated from the slope of the (logarithmic) averages. The fits are normalized to the average equilibrium pressure at 90 °C for $d^{-1} = 0\ nm^{-1}$, indicated by the red dot. Adapted with permission from Ref. [49]. Copyright 2011 WILEY-VCH.

3.1.3. Nanoparticles (Supported or Embedded)

Various materials architecture and synthesis techniques were explored with the aim to solve the sintering and surface contamination issues that affect Mg-based nanostructures during hydrogen sorption cycles. Several authors have studied Mg NPs supported on microporous scaffolds prepared by melt infiltration [45,54–57]; Xia et al. have investigated MgH_2 NPs self-assembled on graphene [58]. These materials always feature very good sorption kinetics, an example of which is shown in Figure 8. However, in those cases where equilibrium data are available, the departure from bulk Mg are minimal [45,54]. An exception is the work of Zhao-Karger et al. who reported markedly decreased enthalpy and entropy from a van 't Hoff plot with only three absorption data points in the 326–351 °C range (see Figure 6 and Ref. [45]). This determination suffers from severe uncertainties as discussed in Section 3.1 and needs confirmation through equilibrium measurements at lower temperatures.

Jeon et al. synthesized an air-stable composite material that consisted of metallic Mg nanocrystals of about 5 nm in a gas-barrier polymer matrix permeable to hydrogen [59]. However, desorption kinetics and thermodynamic data were not provided and the hydrogen sorption properties were rather poor.

Paskevicius et al. employed a clever mecanochemical method to synthesize MgH_2 NPs embedded in a LiCl matrix [14]. The thermodynamic properties were determined accurately, revealing a small but measurable enthalpic bias $(\delta\Delta H^0) = 2.8$ kJ/mol H_2 coupled with an entropy bias $(\delta\Delta S^0) = 3.8$ J/K mol H_2. Hence, the drop of the 1 bar hydrogen equilibrium temperature was only 6 °C compared to bulk Mg. A direct comparison with the prediction of Equation (9) is not possible because the value of $\Delta\gamma$ for the interface with LiCl is not known.

Asano et al. succeeded in embedding nanometer-sized clusters within a TiH_2 matrix by depositing Ti-rich Mg_xTi_{1-x} films and taking advantage of the Mg-Ti mutual immiscibility [60]. The estimated cluster radius was $r \approx 1$ nm, corresponding to ≈ 200 Mg atoms. The absorption and desorption branches of the pressure–transmission isotherms were both shifted upwards with decreasing r (Figure 9a). The sloping plateaus suggested the presence of a wide distribution of cluster sizes.

The amount of destabilization was well explained by Equation (9) assuming the same $\Delta\gamma$ as for Mg films sandwiched within TiH_2 and considering that $A_{nano}/V_{nano} = 3/r$.

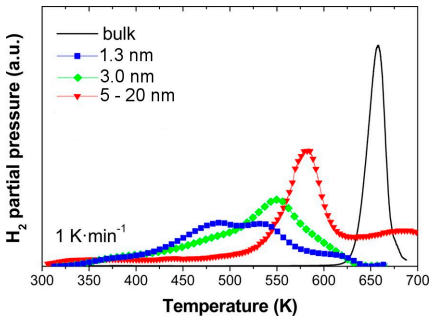

Figure 8. Thermal desorption spectra of MgH_2 NPs of different size confined/supported in a microporous carbon template compared to bulk Mg (black curve). The average size (diameter) of the NPs was obtained from the analysis of bright field electron micrographs. Adapted with permission from Ref. [56]. Copyright 2015 American Chemical Society.

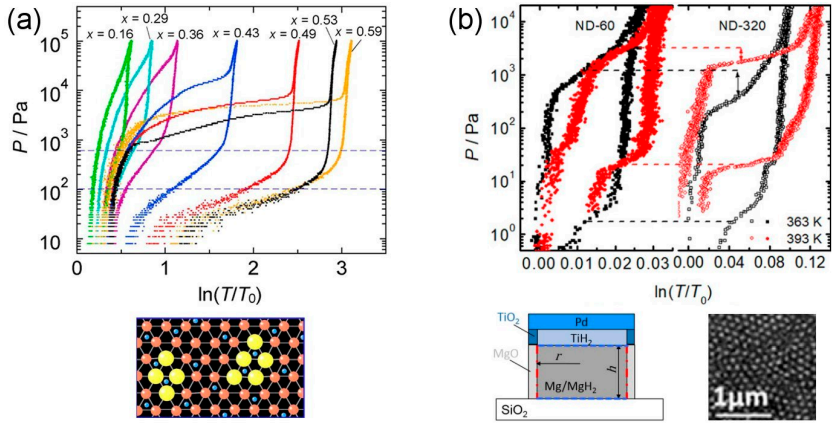

Figure 9. Pressure-optical transmission isotherms on fully embedded Mg nano-objects. (**a**) Mg_xTi_{1-x}-H_2 systems at 120 °C: for small x, Mg or MgH_2 nanoclusters were embedded in a TiH_2 matrix (yellow atoms in the schematic bottom image, estimated cluster radius was ≈ 1 nm). The dashed lines indicate the hydrogen absorption and desorption pressures for a 60 nm thick Mg film. Reprinted with permission from Ref. [60]. Copyright 2015 American Chemical Society; (**b**) Mg (30 nm)/Ti (5 nm)/Pd (5 nm) nanodots (see sketch and electron microscopy image at the bottom) with different diameters 2*r* = 60 (ND-60) and 320 nm (ND-320). The black (red) points were measured at 90 °C (120 °C). Adapted with permission from Ref. [35]. Copyright 2016 Hydrogen Energy Publications LLC.

Molinari et al. employed template-assisted molecular beam epitaxy to deposit highly ordered, monodisperse Mg/Ti/Pd nanodots on SiO_2 substrates coated by a porous ultra-thin alumina membrane [35]. After exposure to air and then to hydrogen, the Mg core of these nanodots was in contact with different phases as schematized in Figure 9b. Pressure-transmission isotherms were measured at 90 and 120 °C on nanodots with diameters of 60 and 320 nm. Figure 9b shows that the desorption plateau pressure did not depend on the nanodots size, whereas the absorption plateau pressure was larger in smaller nanodots. The equilibrium pressure (geometric average of absorption and desorption) of the large nanodots was very close to bulk Mg, whereas small nanodots showed almost a 2-fold increase (Figure 6). The authors suggested that this destabilization arises only in part from interface effects because the nanodots size is rather large, and attributed it mainly to the elastic constraint against nanodots expansion imposed by the surrounding phases [35]. The comparison of the experimental destabilization with the outcome of Equation (12) makes it possible to estimate that

the hydride nanodots experience a compressive elastic strain of about 0.8%. This small value indicates that significant plastic deformation must develop to accommodate the large volume variation (32%) that takes place upon hydride formation/decomposition. The plasticity hampers the achievement of a true destabilization, i.e., of a situation, in which also the desorption pressure increases. In fact, the large hysteresis induced by plastic work shifts the desorption plateau pressure in the undesired direction below the value of quasi-free bulk-like Mg [35,49]. This example in constrained systems shows that the correct assessment of hydride destabilization cannot be gained only from absorption data and highlights the importance of recording the full absorption–desorption isotherm.

Shegai and Langhammer were able to measure an absorption isotherm at 80 °C on a single Mg nanodots sandwiched between TiH_2 layers by using nanoplasmonic spectroscopy [61]. This technique opens exciting opportunities for the characterization of H-sorption thermodynamics at the single particle level and has recently been applied to determine enthalpy and entropy of hydride formation in individual palladium NPs as a function of size and shape [62].

3.2. Mg-Pd Nanomaterials

The main features of the Mg-Pd system are:

- The Mg-Pd binary phase diagram is a rather complex one. Nine intermetallic compounds, with increasing Pd content from Mg_6Pd to MgPd, populate the Mg-rich region (<50 at.% Pd) [63].
- Both Mg and Pd form a binary hydride. $PdH_{0.6}$ is the prototypical interstitial metallic hydride: its enthalpy of formation is −37 kJ/mol H_2 (i.e., much less stable than MgH_2) and its H-sorption kinetics are extremely fast also at room temperature.
- There is no evidence of ternary Mg-Pd-H phases.

In the bulk form, the reaction of $Mg_{1-x}Pd_x$ alloys with H_2 may include different sequential steps depending on the initial stoichiometry and H_2 pressure. For example, starting from the Mg-richest compound Mg_6Pd, the following disproportionation reactions take place with increasing hydrogen pressure, giving rise to three distinct pressure plateaus [64]:

$$Mg_6Pd + 2.35H_2 \rightarrow Mg_{3.65}Pd + 2.35MgH_2. \quad (16)$$

$$Mg_{3.65}Pd + 2.35MgH_2 + 1.15H_2 \rightarrow (1/2)Mg_5Pd_2 + 3.5MgH_2. \quad (17)$$

$$(1/2)Mg_5Pd_2 + 3.5MgH_2 + 1.5H_2 \rightarrow MgPd + 5MgH_2. \quad (18)$$

With respect to Mg_6Pd, the combination of reactions (16) and (17) yields a hydrogen storage capacity of 2.8 wt%, and reaction (18) conveys an additional 1.2 wt%. Even if Pd is too expensive to be integrated in a future application for hydrogen storage, it is often employed as catalyst in Mg-based materials. In thin films, a Pd capping layer also increases the oxidation resistance [65,66]. It is therefore extremely important to take into account the possible formation of intermetallic Mg-Pd phases and the occurrence of reactions (16)–(18) when describing the hydrogen sorption properties of Mg-Pd nanomaterials.

3.2.1. Interfacial Mg-Pd Alloys in Pd-Catalyzed Mg Thin Films and NPs

Pd-capped Mg thin films have been around for quite a while: already in 1990, Krozer and Kasemo studied their H-sorption equilibrium properties at T < 100 °C [67], obtaining different enthalpies for hydride formation (−60.7 ± 6.3 kJ/mol H_2) and decomposition (71 ± 4 kJ/mol H_2) and highlighting the presence of a large pressure hysteresis. Almost 20 years later, Griessen and coworkers pointed out the existence of a linear relationship of the form:

$$1/\ln(p_{abs}/p_0) = a + bd, \quad (19)$$

where p_{abs} is the absorption plateau pressure (measured at 60 °C) and d the thickness of the Mg layer [34]. In the thinnest films with d = 20 nm p_{abs} reached a remarkably high value, about 200 times larger than the pressure at which coexistence of α and β phases appears in bulk Mg upon hydrogen loading. A similar picture was observed with a capping layer of Ni but not of elements that are immiscible with Mg, i.e., Nb, V, and Ti. These results were attributed to an elastic constraint imposed by the capping layer against the expansion of the film and the parameters a and b in Equation (19) were expressed in terms of the elastic constants of Mg and of the capping metal [34]. The authors argued that the constraint is effective only when the capping layer and Mg are miscible, so that the interfaces are elastically stiff.

There are two interrelated problems in the above interpretation. The first is the amount of strain needed to explain the observed pressure increase. Clemens and coworkers showed that the stress measured during hydrogenation of Mg/Pd films corresponds to a negligible increase in equilibrium pressure [68], whereas the 200-fold increase observed by Griessen and coworkers would require a linear strain of ~13% [34,68]. This is one order of magnitude higher than typical thin film strains and it is not physically reasonable that such a large strain can exist in MgH_2. Clemens and coworkers suggested that the observed pressure increase originates with the thermodynamics of the intermixing region that may follow reaction paths (16)–(18). They analyzed the Mg/Pd interfaces by transmission electron microscopy (Figure 10) and developed a thermodynamic model of the effect of alloying on equilibrium pressure, showing that its increase was consistent with the observed thickness of the intermixed region [68]. The second problem is that the large thermodynamical bias was claimed only from the upward shift of the absorption plateau. The elastic constraint model predicts that the desorption plateau should also be similarly shifted, but subsequent measurements showed that this was not the case [52]. Again, the presence of a large hysteresis did not make it possible to achieve a true destabilization of the hydride and induced large errors in the determination of thermodynamic parameters from absorption data only.

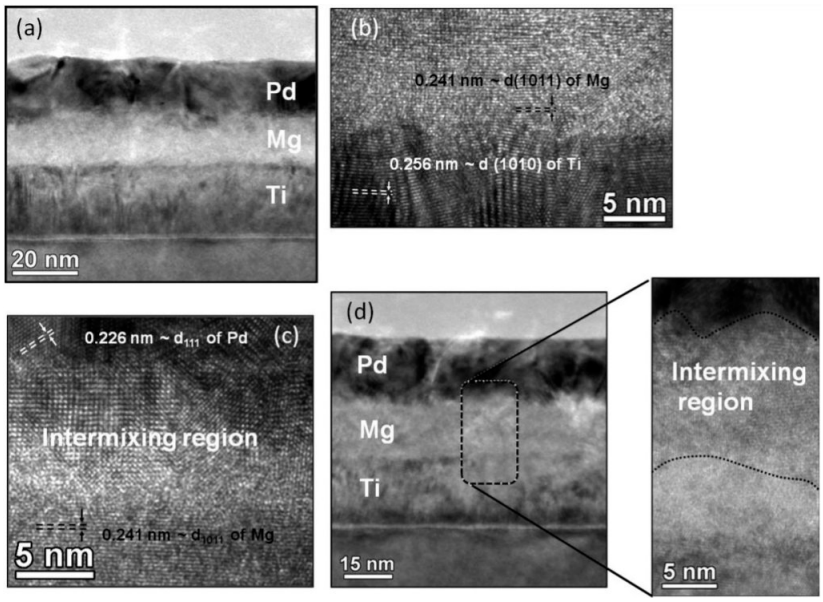

Figure 10. (**a**) Cross-section TEM image of as-deposited Ti/Mg/Pd multilayer samples; (**b**) High Resolution TEM (HRTEM) image of the Ti/Mg interface in (**a**); (**c**) HRTEM image of the Mg/Pd interface in (**a**); (**d**) Cross-section TEM image and HRTEM of annealed Ti/Mg/Pd sample. The dashed area highlights the intermixing region. Reprinted with permission from Ref. [68]. Copyright 2012 American Physical Society.

The issue of Mg-Pd alloying at interfaces in nanomaterials and the disproportionation reactions (16)–(18) were studied in relatively large (~400 nm) Mg NPs decorated by Pd clusters on top of the native MgO surface layer [69–71]. The overall composition of these NPs was tuned between 1 and 3.3 at.% Pd. During a heating ramp at 15 °C/min, Pd began to react with Mg forming Mg_5Pd_2 at about 220 °C, despite the 4 nm thick MgO separation layer. With increasing temperature, pure Pd disappeared and Mg_6Pd replaced Mg_5Pd_2, until a Mg-Mg_6Pd two-phase field was attained, in agreement with the phase diagram region at low Pd content. This irreversible reaction was tracked by in situ synchrotron radiation powder X-ray diffraction (SR-PXD) [70] and by X-ray absorption spectroscopy (XAS) at the Pd K-edge (Figure 11) [71]. The same techniques were employed to identify the reaction paths: upon absorption at 300 °C and $p(H_2)$ = 10 bar, the disproportionation of Mg_6Pd led to the formation of Mg_3Pd and Mg_5Pd_2 phases along with MgH_2. At 50 bar, SR-PXD and XAS showed the presence of the cubic MgPd phase. The slightly expanded lattice parameter was compatible with a solid solution $MgPdH_\delta$ with δ in the range 0.4–0.6. These reactions were fully reversible with decreasing pressure as shown in Figure 11, focused on the local atomic environment around Pd. Hydrogen sorption by Mg-Pd alloys proceeds in parallel with hydrogen sorption by Mg, which is the majority phase in the composite NPs. Due to the low amount of Pd, it was not possible to clearly detect different plateau pressures for Mg (reaction (1)) and for Mg-Pd alloys (reactions (16)–(18)). For the hydrogenation of Mg_6Pd, Fernandez et al. have calculated that the enthalpy becomes less negative with increasing Pd content of the final intermetallic compound, going from −75.3 kJ/mol H_2 for Mg_3Pd to −69.1 kJ/mol H_2 for MgPd [72]. The maximum storage capacity of the Mg-Pd NPs was about 5.5 wt% for samples with 1 at.% Pd.

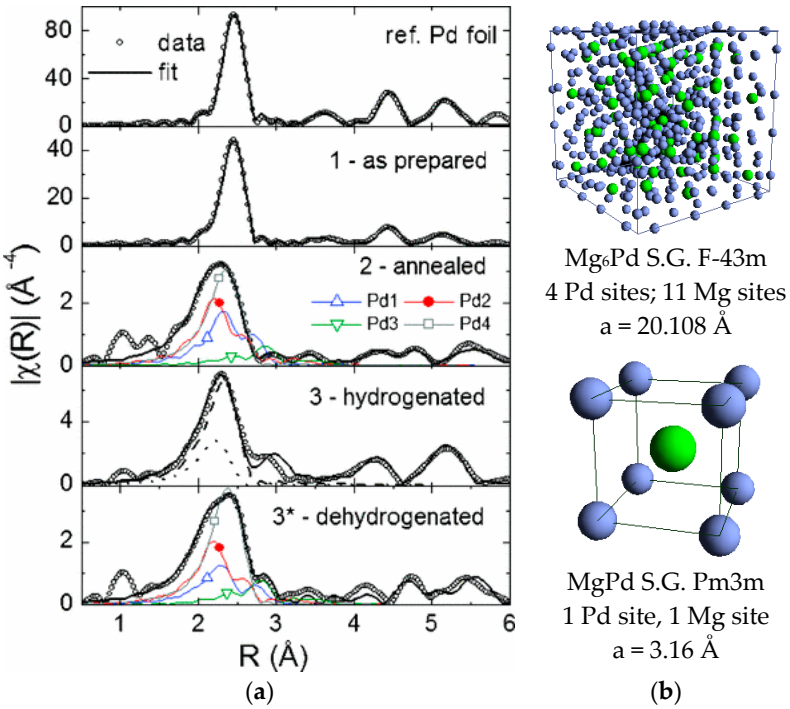

Figure 11. Local structure around Pd in Mg-Pd NPs. (**a**) Magnitude of the Fourier Transform of raw Extended X-ray Absorption Fine Structure (EXAFS) spectra at the Pd K-edge (open circles) and corresponding fit (thick solid lines). In the graphs of sample 2 and 3*, the first-shell-like contributions from the four different Pd sites in the Mg_6Pd structure are displayed as thin solid lines marked by one symbol. Adapted with permission from Ref. [71]. Copyright 2011 American Physical Society. (**b**) Crystal structures of the intermetallic compounds Mg_6Pd and MgPd.

3.2.2. Nanoconfined Mg-Pd Compounds

Mg_6Pd NPs of 4 nm were obtained by infiltration of Mg on previously formed Pd NPs dispersed within the pores of porous carbon [73]. EXAFS analysis showed that the NPs had a simpler crystallographic arrangement and a higher atomic disorder compared to the bulk. A change in the plateau pressure (Figure 12) indicating thermodynamic destabilization of the hydride phase was reported along with faster kinetics were. This modification of the sorption properties was ascribed both to the small particle size and to the difference in the crystal structure compared to that of bulk Mg_6Pd.

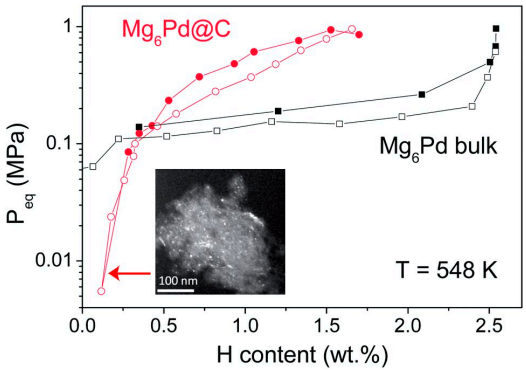

Figure 12. Hydrogen sorption isotherms at 548 K for bulk (black line) and nanoconfined (red line, TEM image in the inset) Mg_6Pd. Filled and empty symbols stand for absorption and desorption isotherm curves, respectively. Reprinted with permission from Ref. [73]. Copyright 2014 The Royal Society of Chemistry.

3.3. Mg-Ni Nanomaterials

The addition of Ni to the Mg system can improve the hydrogen sorption properties for two reasons. The first is that Ni is an excellent (de)hydrogenation catalyst, meaning that it easily adsorbs and dissociates H_2 molecules (and vice versa). The second is related to alloy formation. The essential features of the Mg-Ni system are:

- Mg and Ni form two stable line compounds, i.e., Mg_2Ni and $MgNi_2$. The solubility of Mg in Mg_2Ni and of Ni in $MgNi_2$ are negligible.
- $MgNi_2$ can form the hydride $MgNi_2H_3$ only at very high pressure, i.e., 28 kbar at 300 °C [12].
- Mg_2Ni forms the complex ternary hydride Mg_2NiH_4, in which covalently bonded $[NiH_4]^{4-}$ complexes are ionically bonded to Mg^{2+}. The formation enthalpy is −64 kJ/mol H_2, still quite high but more favorable than MgH_2 as far as hydrogen desorption is concerned.

Clearly, the presence of Ni significantly lowers the gravimetric H-storage capacity from 7.6 wt% of MgH_2 down to 3.6 wt% of Mg_2NiH_4. For this reason, many researchers focused on $Mg_{1-x}Ni_x$ alloys with $x \leq 0.33$ with the aim to improve the H-sorption properties without sacrificing the weight capacity too much. Akiba and coworkers studied glassy, nanostructured and crystalline $Mg_{1-x}Ni_x$ alloys with five different compositions ($x \leq 0.33$) prepared by rapid quenching with the melt-spinning method [74]. Orimo and Fujii studied Mg-Ni alloys with higher Ni content between Mg_2Ni and $MgNi_2$ including an amorphous MgNi alloy obtained by ball milling [75]. DFT calculations suggested that Ni dopant incorporated in the MgH_2 lattice destabilizes the hydride improving hydrogen desorption thermodynamics [29,38]. However, Mg-rich $Mg_{1-x}Ni_x$ alloys are metastable and split into Mg-Mg_2Ni two-phase fields upon heating. Several studies on different types of Mg-Mg_2Ni nanocomposites suggested that the better kinetics of the Mg_2Ni/Mg_2NiH_4 system promote H-sorption from Mg/MgH_2 if the phases are intimately mixed at the nanoscale [76–79]. This is mainly a kinetic improvement that does not alter the equilibrium thermodynamics of MgH_2 and Mg_2NiH_4. In fact, Zou et al. have

measured two distinct pressure plateaus in the PCIs of Mg-rich Mg-Ni fine particles, obtaining the same thermodynamic parameters as for the bulk individual phases [80].

Recent developments are related to further insight into the properties of Mg-Ni alloys at the nanoscale by studying thin films [81], freestanding NPs [78,82] and NPs supported on microporous scaffolds [83,84]. Matsuda et al. observed hydrogen absorption by Mg-Ni thin films in situ with an environmental transmission electron microscope. First, nucleation and growth of Mg_2NiH_4 crystals in an Mg-rich amorphous matrix occurred, followed by crystallization of MgH_2, demonstrating how the presence of Mg_2Ni facilitated the hydrogenation of Mg [81]. Callini et al. performed in situ SR-PXD experiments to follow Mg-Ni alloying and hydride formation/decomposition in Mg NPs surface-decorated with 10 wt% Ni [78]. They showed that Ni, Mg_2Ni and Mg_2NiH_4 play a catalytic role for the Mg-MgH_2 metal-hydride transformation achieving remarkably fast kinetics. Zlotea et al. infiltrated a Mg-rich Mg-Ni nanoalloy in microporous carbon, obtaining both Mg and Mg_2Ni confined NPs. Hydrogen absorption/desorption of nano-Mg_2Ni was reversible and sorption kinetics were very fast (~5 min at 483 K). On the contrary, the thermodynamic properties were not modified by nanoconfinement [84].

3.4. Mg-Ti Nanomaterials

The Mg-Ti system provides another interesting case study with distinctive features not shared by the previously discussed Mg-Pd and Mg-Ni:

- Mg and Ti are completely immiscible in the solid-state; there are no stable compounds with intermediate stoichiometry, although metastable Mg-Ti solid solutions and compounds have been obtained by ball milling [85,86] and by physical co-deposition of mixed Mg-Ti vapors from two independent sources [87–90];
- Ti forms the highly stable TiH_2 hydride ($\Delta H^0 \approx -140$ kJ/mol H_2). This means that TiH_2 will never decompose under the experimental conditions used to study hydrogen sorption in Mg.

Notten and coworkers reported on the excellent hydrogen storage capacity of Mg_yTi_{1-y} thin films (with $0.50 \leq y \leq 0.95$), which is approximately five times larger than that of conventional metal hydride electrodes in NiMH batteries [91]. The best performances were obtained with the $Mg_{0.80}Ti_{0.20}$ alloy that reached a reversible hydrogen storage capacity of ~6.5 wt%. Furthermore, galvanostatic hydrogenation of the Mg_yTi_{1-y} alloys revealed the formation of products that do not correspond to the intrinsic thermodynamic properties of the individual Mg and Ti hydride. This finding and the shift of Mg Bragg peaks with increasing Ti content indicated that strong segregation did not take place and that Mg and Ti were intimately mixed (Figure 13a). These films also exhibited remarkable optical properties, being highly reflective in the metallic state and strongly optically absorbing upon hydrogen loading [87]. Notably, the transition between reflective and absorbing state was reversible and controllable through the hydrogen pressure, opening possible applications of the material as smart solar collector. The high optical absorption hinted at the coexistence of a metallic and a semiconducting phase. Advanced structural investigations by XRD and EXAFS revealed the presence of a chemically partially segregated but structurally coherent metastable phase [92]. The robustness of the material and its exceptional properties were attributed to the formation of nanoscale compositional modulation in the intermetallic alloy.

TiH_2 finely dispersed within Mg/MgH_2 by ball-milling techniques greatly speeds up the hydrogen sorption kinetics [46,47]. The equilibrium pressure-temperature data are, on the other hand, very close to bulk Mg, as shown in Figure 6, suggesting that little or no change of the thermodynamics takes place. The outstanding kinetic properties were attributed to the limited grain growth of Mg and MgH_2 phases, the coherent coupling between TiH_2 and Mg/MgH_2, and the fast H-diffusion through sub-stoichiometric $MgH_{2-\eta}$ and $TiH_{2-\eta}$ phases [93]. The remarkable influence of TiH_2 on the H-sorption kinetics was also observed in MgH_2-TiH_2 composite NPs already mentioned in Section 3.1.1 [94]. The combination of high surface area, small particle size and nanoscale dispersion

of TiH_2 made it possible to measure equilibrium and kinetic properties of the Mg/MgH_2 system down to 70 °C without using Pd as capping or catalyst layer [48]. Prior to hydride formation, the NPs consisted in a hcp metastable Mg-Ti solid solution up to ~15 at.% Ti, as demonstrated by high resolution elemental mapping (Figure 13b) and X-ray diffraction [89]. Krishnan et al. also observed that bimetallic Mg-Ti NPs grown by gas-phase condensation have better thermal stability against void formation (Nanoscale Kirkendall effect) and Mg evaporation [95]. Recent XRD and XPS studies showed that the TiH_2 phase remains unchanged during hydrogen desorption from MgH_2 without formation of intermediates [96]. In all these $(MgH_2)_y$—$(TiH_2)_{1-y}$ (nano)composites, the reversible hydrogen storage capacity originates only from the $Mg+H_2 \leftrightarrow MgH_2$ reaction because TiH_2 is stable at the applied pressure-temperature conditions. The composites with y = 0.7 and y = 0.9 showed reversible capacities of ~3.7 wt% [46] and ~6.0 wt% [47], respectively, with excellent stability upon hydrogen cycling.

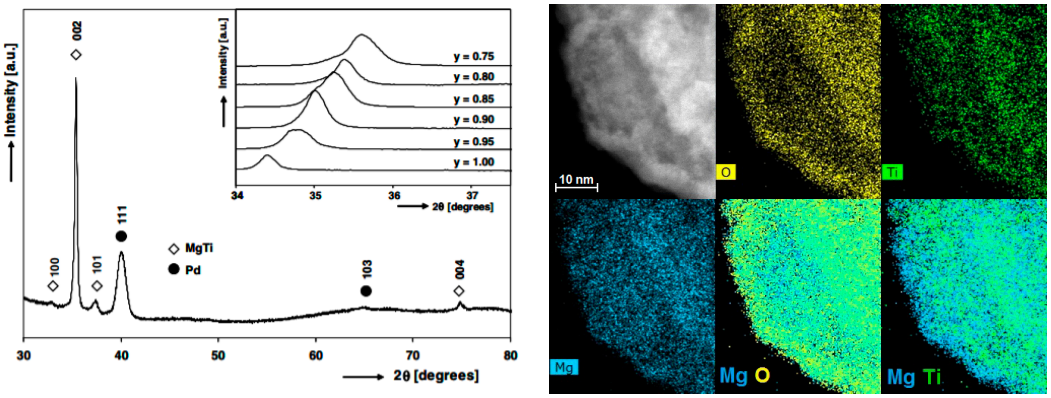

(**a**) (**b**)

Figure 13. (**a**): XRD profiles of a 200-nm thick $Mg_{0.80}Ti_{0.20}$ thin film, capped with 10 nm of Pd. Indicated are the reflections and orientations of the different layers. The inset shows the evolution of the (002) reflections of $Mg_yTi_{(1-y)}$ alloys with y ranging from 0.75 to 1.00. Reprinted with permission from Ref. [91]. Copyright 2005 Elsevier B.V. (**b**): Scanning TEM image (top left) and energy-dispersive X-ray mapping of Mg-Ti NPs prepared by gas-phase condensation. The O, Ti and Mg signals are shown in yellow, green and blue, respectively. Ti atoms are dispersed in the core of the NPs while a MgO shell is formed after exposure to the air. Reprinted with permission from Ref. [89]. Copyright 2016 The Royal Society of Chemistry.

3.5. Other Mg-X Nanomaterials

Reactions schemes (13)–(15) and their combinations have been applied to a variety of Mg-X alloys and compounds, with X a *p*-element (Al, Si, Ge, Sn, In) or a *d*-element (e.g., Co, Fe, Zn, Nb, besides the previously discussed Pd, Ni and Ti). The reaction enthalpy can be changed in both directions, whereas the gravimetric hydrogen capacity invariably decreases. The interested reader is referred to a recent exhaustive review on the subject [12]. Most of these studies did not focus on the nanoscale-specific features that can influence the thermodynamics, although the samples were often nanocrystalline alloys or nanocomposites prepared by ball milling in order to improve diffusion kinetics.

Shao et al. have studied the hydrogen sorption properties of pure Mg and Mg-X NPs (with X = Ni, Co, Cu in a 2:1 Mg:X molar ratio) prepared by hydrogen plasma metal reactions [97]. The Mg-X NP mixtures were heated at 350–400 °C and hydrogenated, yielding Mg_2NiH_4, Mg_2CoH_5 and $3MgH_2 + MgCu_2$ hydride systems. Hydrogen release under vacuum at the same temperature led to the formation of Mg_2Ni, $Mg_xCo + (2 - x)Mg$, and Mg_2Cu metallic systems. The same approach was adopted for the synthesis of nanostructured Mg_2FeH_6 [98], which transforms into 2Mg + Fe upon hydrogen desorption. The Mg and Mg_2X NPs exhibited good sorption kinetics without change of thermodynamics compared to bulk systems with the same composition. This is not surprising since

the NPs were rather large (50–200 nm). In order of desorption enthalpy, the hydride systems can be classified as: $Mg_2CoH_5 \approx Mg_2FeH_6 > MgH_2 > 3MgH_2 + MgCu_2 > Mg_2NiH_4$ [97,98].

Aguey-Zinsou and coworkers prepared Mg NPs partially coated with Co, Fe, Ni, Si, and Ti using electroless reduction followed by a transmetalation process [99]. The formation of transition metal complex hydrides was observed at temperatures above 350 °C. The shell formed by these hydrides around the Mg/MgH_2 core seemed to have a little but measurable effect on the equilibrium pressure, which decreased from 4.4 bar for the uncoated NPs down to 3.6 bar for the Ni-coated ones. The equilibrium pressure for Fe, Co, Si and Ni suggested a possible correlation with the Pauling electronegativity of the elements [99].

Nb and Nb_2O_5 have been extensively studied as additives that greatly enhance hydrogen sorption kinetics of Mg/MgH_2 [100,101]. Mg and Nb are strongly immiscible and do not form stable compounds. Nevertheless, the possibility to obtain a metastable bcc $Mg_{0.75}Nb_{0.25}$ compound was recently demonstrated by physical co-deposition of Mg and Nb with the appropriate stoichiometry [102]. Various structures of Mg-Nb compounds calculated by DFT are shown in Figure 14. The bcc $Mg_{0.75}Nb_{0.25}$ alloy transformed into a metastable hydride $Mg_{0.75}Nb_{0.25}H_2$ upon exposure to hydrogen at room temperature. This new metal–hydrogen system had an enthalpy of hydride formation of −53 kJ/mol H_2, indicating a significant thermodynamic destabilization compared to MgH_2, and a maximum reversible storage capacity of 4 wt%. The system was unstable when cycled at temperatures above 150 °C and decomposed into MgH_2 and NbH.

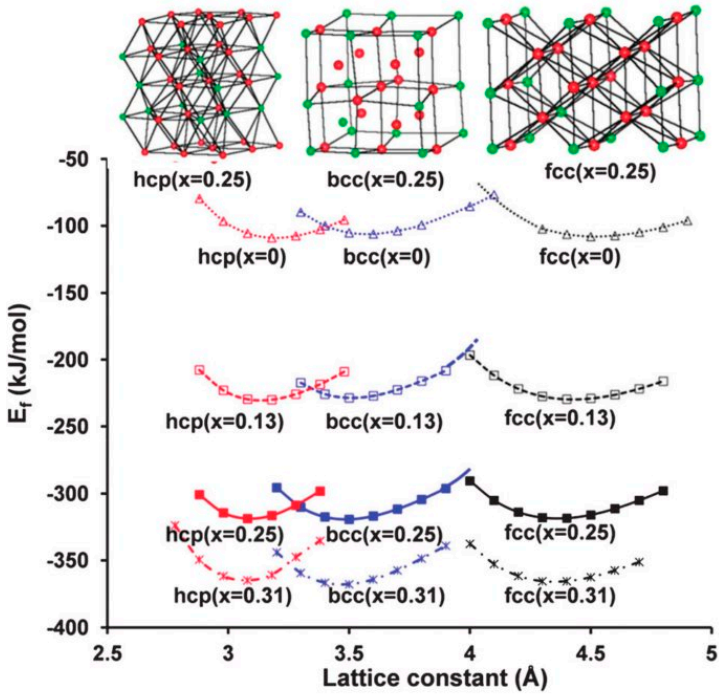

Figure 14. Formation energies of $Mg_{1-x}Nb_x$ (x = 0, 0.13, 0.25 and 0.31) with various structures as a function of lattice constant. The hcp, bcc and fcc unit cells for $Mg_{0.75}Nb_{0.25}$ are shown, with Nb atoms being the green spheres. Reprinted with permission from Ref. [102]. Copyright 2012 Royal Society of Chemistry.

Also V and its oxides improve significantly the H-sorption kinetics of Mg/MgH_2 [103–105]. Mg and V do not form compounds and are strongly immiscible; therefore, thermodynamic tuning by alloying cannot be achieved. The formation of a ternary Mg_6VH_x hydride with fcc structure from a mixture of MgH_2 and V was observed at high pressure (8 GPa) at 600 °C [106]. The free energy of the

interfaces between Mg/MgH_2 and V/VH_x or Nb/NbH_x are not know: I speculate that this may be an interesting subject for experimental and theoretical investigations.

4. Conclusions

In this review, I examined the thermodynamics of hydride formation and decomposition in nanomaterials, with particular emphasis on NPs (free or supported/embedded) and thin films. The results of calculations based on density functional theory were quantitatively compared with the experimental values of the reaction enthalpy and entropy in Mg-based metallic nanomaterials. The major points emerged from this comparison are summarized in the following.

- Theoretical works predicted that $(\delta\Delta H^0)^{sur}$ increases with decreasing size of MgH_2 NPs, reaching $\approx$5 kJ/mol H_2 for a radius of 1 nm [27]. For even smaller MgH_2 clusters with less than 10 Mg atoms, contrasting calculations were published: the most recent ones suggest that a stabilizing reconstruction takes place [28–30]. However, these ultra-small sizes have eluded experimental verification and are of little practical interest.
- Experiments on larger NPs (up to 15 nm diameter) sometimes yielded $(\delta\Delta H^0)^{sur} \approx 15$ kJ/mol H_2, far above the theoretical predictions [43,45,99]. These large values came only from measurements carried out in a narrow temperature range above 300 °C where the NPs were not stable. Moreover, sometimes only absorption data were reported. A true destabilization was not obtained because the equilibrium temperature for $p(H_2) = 1$ bar remained very close to the value of bulk Mg ($\approx$283 °C). The authors attributed this to an entropy compensation effect, $(\delta\Delta S^0)^{sur} \approx 15$ J/K mol H_2. However, it is well known that van 't Hoff analysis on a narrow temperature range can give rise to phantom enthalpy–entropy correlations.
- Our recent measurements down to 70 °C on MgH_2/TiH_2 composite NPs showed tiny variations of the equilibrium pressure compared to the extrapolated values of bulk Mg. We obtained a value $(\delta\Delta H^0)^{sur} \approx 6$ kJ/mol H_2 that is compatible with the calculations. These experiments ruled out the presence of a large enthalpy bias in Mg NPs with a diameter $\geq$ 10 nm.
- Low temperature experiments (90–200 °C) on Mg thin films are in good agreement with the interface destabilization model described by Equations (9) and (10), the essential parameter of which is the difference $\Delta\gamma$ between the specific interface free energy in the hydride and in the metal phase [49]. The experimental value for Mg/MgH_2 films sandwiched within TiH_2 is $\Delta\gamma = 0.33$ J/m^2, while calculations give $\Delta\gamma$ (0 K) = $\Delta h \approx$ 0.5–0.6 J/m^2. The difference may be due to the negative entropic contribution $-T\Delta\sigma$. At 90 °C, in a 2 nm film, the measured thermodynamical bias was $(\delta\Delta G^0)^{int} = 4.6$ kJ/mol H_2, corresponding to a 5-fold pressure increase. A similar effect was observed in MgH_2 clusters embedded in a TiH_2 matrix.
- Calculations and experimental data on the interface/surface entropy are lacking. Knowledge of the $\Delta\sigma$ of interfaces between metal hydrides and different materials may prove useful for the tailoring of their thermodynamics. I suggest that this may be a prolific research direction both to improve the current understanding of nanoscale thermodynamics and to better control hydride properties towards applications.
- In order to prove the destabilization of the hydride it is necessary to measure the *desorption* plateau. In a truly destabilized hydride, an upward shift should be observed. Conversely, in Mg nanostructures, an upward shift of only the *absorption* plateau was frequently reported [33–35]. This may simply be caused by a large pressure hysteresis. Any destabilization claims and any enthalpy/entropy results based solely on the absorption plateau pressures are unreliable.
- In elastically constrained systems, the stresses that build up during volume expansion exceed the yield point of the material, leading to plastic rather than elastic strain. Plasticity is coupled with a large pressure hysteresis. The bias associated with the small elastic strain induces only a tiny shift of the average equilibrium pressure [35,68]. For this reason, a practical destabilization of MgH_2 by elastic constraint has not yet been achieved.

- The spatial distribution of phases in small nanoparticles that individually undergo reaction schemes (13)–(15) is relatively unexplored. I believe that this may be a fruitful subject for future structural/thermodynamic calculations and experiments.
- TiH_2 is an excellent partner of Mg/MgH_2, making it possible to grow quasi-free films and composite NPs with very small hysteresis. Furthermore, it greatly speeds up the hydrogen sorption kinetics. Further studies are needed in order to unravel the detailed microscopic mechanisms behind its "catalytic" action.

Acknowledgments: The financial support from European Cooperation in Science and Technology (COST), Action MP1103 "Nanostructured materials for solid-state hydrogen storage", is gratefully acknowledged.

Conflicts of Interest: The author declares no conflict of interest.

References

1. Takagi, S.; Orimo, S.-I. Recent progress in hydrogen-rich materials from the perspective of bonding flexibility of hydrogen. *Scr. Mater.* **2015**, *109*, 1–5. [CrossRef]
2. Schlapbach, L.; Züttel, A. Hydrogen-storage materials for mobile applications. *Nature* **2001**, *414*, 353–358. [CrossRef] [PubMed]
3. Eberle, U.; Felderhoff, M.; Schüth, F. Chemical and physical solutions for hydrogen storage. *Angew. Chem. Int. Ed.* **2009**, *48*, 6608–6630. [CrossRef] [PubMed]
4. Yoshimura, K.; Langhammer, C.; Dam, B. Metal hydrides for smart window and sensor applications. *MRS Bull.* **2013**, *38*, 495–503. [CrossRef]
5. Lototskyy, M.V.; Yartys, V.A.; Pollet, B.G.; Bowman, R.C. Metal hydride hydrogen compressors: A review. *Int. J. Hydrog. Energy* **2014**, *39*, 5818–5851. [CrossRef]
6. Felderhoff, M.; Bogdanović, B. High temperature metal hydrides as heat storage materials for solar and related applications. *Int. J. Mol. Sci.* **2009**, *10*, 325–344. [CrossRef] [PubMed]
7. Mohtadi, R.; Orimo, S. The renaissance of hydrides as energy materials. *Nat. Rev. Mater.* **2016**, *2*, 16091. [CrossRef]
8. Unemoto, A.; Matsuo, M.; Orimo, S. Complex hydrides for electrochemical energy storage. *Adv. Funct. Mater.* **2014**, *24*, 2267–2279. [CrossRef]
9. Oumellal, Y.; Rougier, A.; Nazri, G.A.; Tarascon, J.-M.; Aymard, L. Metal hydrides for lithium-ion batteries. *Nat. Mater.* **2008**, *7*, 916–921. [CrossRef] [PubMed]
10. Jain, I.P.; Lal, C.; Jain, A. Hydrogen storage in Mg: A most promising material. *Int. J. Hydrog. Energy* **2010**, *35*, 5133–5144. [CrossRef]
11. Crivello, J.-C.; Dam, B.; Denys, R.V.; Dornheim, M.; Grant, D.M.; Huot, J.; Jensen, T.R.; de Jongh, P.; Latroche, M.; Milanese, C.; Milčius, D.; et al. Review of magnesium hydride-based materials: Development and optimisation. *Appl. Phys. A Mater. Sci. Process.* **2016**, *122*. [CrossRef]
12. Crivello, J.-C.; Denys, R.V.; Dornheim, M.; Felderhoff, M.; Grant, D.M.; Huot, J.; Jensen, T.R.; de Jongh, P.; Latroche, M.; Walker, G.S.; Webb, C.J.; et al. Mg-based compounds for hydrogen and energy storage. *Appl. Phys. A* **2016**, *122*, 85. [CrossRef]
13. Stampfer, J.F.; Holley, C.E.; Suttle, J.F. The magnesium-hydrogen system. *J. Am. Chem. Soc.* **1960**, *82*, 3504–3508. [CrossRef]
14. Paskevicius, M.; Sheppard, D.A.; Buckley, C.E. Thermodynamic Changes in Mechanochemically Synthesized Magnesium Hydride Nanoparticles. *J. Am. Chem. Soc.* **2010**, *6*, 469–472. [CrossRef] [PubMed]
15. Lototskyy, M.V.; Tolj, I.; Pickering, L.; Sita, C.; Barbir, F.; Yartys, V. The use of metal hydrides in fuel cell applications. *Prog. Nat. Sci. Mater. Int.* **2017**, *27*, 3–20. [CrossRef]
16. Gremaud, R.; Broedersz, C.P.; Borsa, D.M.; Borgschulte, A.; Mauron, P.; Schreuders, H.; Rector, J.H.; Dam, B.; Griessen, R. Hydrogenography: An optical combinatorial method to find new light-weight hydrogen-storage materials. *Adv. Mater.* **2007**, *19*, 2813–2817. [CrossRef]
17. Buschow, K.H.J.; Bouten, P.C.P.; Miedema, A.R. Hydrides formed from intermetallic compounds of two transition metals: A special class of ternary alloys. *Rep. Prog. Phys.* **2000**, *45*, 937–1039. [CrossRef]

18. Callini, E.; Aguey-Zinsou, K.-F.; Ahuja, R.; Ares, J.R.; Bals, S.; Biliškov, N.; Chakraborty, S.; Charalambopoulou, G.; Chaudhary, A.-L.; Cuevas, F.; Dam, B.; et al. Nanostructured materials for solid-state hydrogen storage: A review of the achievement of COST Action MP1103. *Int. J. Hydrog. Energy* **2016**, *41*, 14404–14428. [CrossRef]
19. Van Wees, B.J.; van Houten, H.; Beenakker, C.W.J.; Williamson, J.G.; Kouwenhoven, L.P.; van der Marel, D.; Foxon, C.T. Quantized conductance of point contacts in a two-dimensional electron gas. *Phys. Rev. Lett.* **1988**, *60*, 848–850. [CrossRef] [PubMed]
20. Pasquini, L.; Rempel, A.A.; Würschum, R.; Reimann, K.; Müller, M.A.; Fultz, B.; Schaefer, H.-E. Thermal vacancy formation and $D0_3$ ordering in nanocrystalline intermetallic $(Fe_3Si)_{95}Nb_5$. *Phys. Rev. B Condens. Matter Mater. Phys.* **2001**, *63*. [CrossRef]
21. Hammer, B.; Norskov, J.K. Electronic factors determining the reactivity of metal surfaces. *Surf. Sci.* **1995**, *343*, 211–220. [CrossRef]
22. Pasquini, L.; Barla, A.; Chumakov, A.I.; Leupold, O.; Rüffer, R.; Deriu, A.; Bonetti, E. Size and oxidation effects on the vibrational properties of nanocrystalline α-Fe. *Phys. Rev. B Condens. Matter Mater. Phys.* **2002**, *66*. [CrossRef]
23. Calvo, F. Thermodynamics of nanoalloys. *Phys. Chem. Chem. Phys.* **2015**, *17*, 27922–27939. [CrossRef] [PubMed]
24. Bérubé, V.; Radtke, G.; Dresselhaus, M.; Chen, G. Size effects on the hydrogen storage properties of nanostructured metal hydrides: A. review. *Int. J. Energy Res.* **2007**, *31*, 637–663. [CrossRef]
25. De Jongh, P.E.; Adelhelm, P. Nanosizing and nanoconfinement: New strategies towards meeting hydrogen storage goals. *ChemSusChem* **2010**, *3*, 1332–1348. [CrossRef] [PubMed]
26. Sun, Y.; Shen, C.; Lai, Q.; Liu, W.; Wang, D.-W.; Aguey-Zinsou, K.-F. Tailoring magnesium based materials for hydrogen storage through synthesis: Current state of the art. *Energy Storage Mater.* **2018**, *10*, 168–198. [CrossRef]
27. Kim, K.C.; Dai, B.; Karl Johnson, J.; Sholl, D.S. Assessing nanoparticle size effects on metal hydride thermodynamics using the Wulff construction. *Nanotechnology* **2009**, *20*, 204001. [CrossRef] [PubMed]
28. Wagemans, R.W.P.; Van Lenthe, J.H.; De Jongh, P.E.; Van Dillen, A.J.; De Jong, K.P. Hydrogen storage in magnesium clusters: Quantum chemical study. *J. Am. Chem. Soc.* **2005**, *127*, 16675–16680. [CrossRef] [PubMed]
29. Shevlin, S.A.; Guo, Z.X. MgH2 dehydrogenation thermodynamics: Nanostructuring and transition metal doping. *J. Phys. Chem. C* **2013**, *117*, 10883–10891. [CrossRef]
30. Wu, Z.; Allendorf, M.D.; Grossman, J.C. Quantum Monte Carlo Simulation of Nanoscale MgH_2 Cluster Thermodynamics. *J. Am. Chem. Soc.* **2009**, *131*, 13918–13919. [CrossRef] [PubMed]
31. Tao, S.X.; Notten, P.H.L.; Van Santen, R.A.; Jansen, A.P.J. Fluorite transition metal hydride induced destabilization of the MgH_2 system in MgH_2/TMH_2 multilayers (TM = Sc, Ti, V, Cr, Y, Zr, Nb, La, Hf). *Phys. Rev. B Condens. Matter Mater. Phys.* **2010**, *82*, 1–5. [CrossRef]
32. Hao, S.Q.; Sholl, D.S. Effect of TiH2-induced strain on thermodynamics of hydrogen release from MgH_2. *J. Phys. Chem. C* **2012**, *116*, 2045–2050. [CrossRef]
33. Pasquini, L.; Sacchi, M.; Brighi, M.; Boelsma, C.; Bals, S.; Perkisas, T.; Dam, B. Hydride destabilization in core-shell nanoparticles. *Int. J. Hydrog. Energy* **2014**, *39*. [CrossRef]
34. Baldi, A.; Gonzalez-Silveira, M.; Palmisano, V.; Dam, B.; Griessen, R. Destabilization of the Mg-H system through elastic constraints. *Phys. Rev. Lett.* **2009**, *102*, 1–4. [CrossRef] [PubMed]
35. Molinari, A.; D'Amico, F.; Calizzi, M.; Zheng, Y.; Boelsma, C.; Mooij, L.; Lei, Y.; Hahn, H.; Dam, B.; Pasquini, L. Interface and strain effects on the H-sorption thermodynamics of size-selected Mg nanodots. *Int. J. Hydrog. Energy* **2016**, *41*, 9841–9851. [CrossRef]
36. Cleri, F.; Celino, M.; Montone, A.; Bonetti, E.; Pasquini, L. Experimental and theoretical characterization of the 3D-dopants bias on the H desorption of Mg hydrides. *Mater. Sci. Forum* **2007**, *555*, 349–354. [CrossRef]
37. Hussain, T.; Maark, T.A.; Chakraborty, S.; Ahuja, R. Improvement in hydrogen desorption from β- and γ-MgH_2 upon transition-metal doping. *ChemPhysChem* **2015**, *16*, 2557–2561. [CrossRef] [PubMed]
38. Paskaš Mamula, B.; Grbović Novaković, J.; Radisavljević, I.; Ivanović, N.; Novaković, N. Electronic structure and charge distribution topology of MgH_2 doped with 3D transition metals. *Int. J. Hydrog. Energy* **2014**, *39*, 5874–5887. [CrossRef]

39. Friedrichs, O.; Kolodziejczyk, L.; Sanchez-Lopez, J.C.; Fernandez, A.; Lyubenova, L.; Zander, D.; Köster, U.; Aguey-Zinsou, K.-F.; Klassen, T.; Bormann, R. Influence of particle size on electrochemical and gas-phase hydrogen storage in nanocrystalline Mg. *J. Alloys Compd.* **2008**, *463*, 539–545. [CrossRef]
40. Pasquini, L.; Callini, E.; Piscopiello, E.; Montone, A.; Antisari, M.V.; Bonetti, E. Metal-hydride transformation kinetics in Mg nanoparticles. *Appl. Phys. Lett.* **2009**, *94*. [CrossRef]
41. Krishnan, G.; Kooi, B.J.; Palasantzas, G.; Pivak, Y.; Dam, B. Thermal stability of gas phase magnesium nanoparticles. *J. Appl. Phys.* **2010**, *107*, 1–7. [CrossRef]
42. Norberg, N.S.; Arthur, T.S.; Fredrick, S.J.; Prieto, A.L. Size-Dependent Hydrogen Storage Properties of Mg Nanocrystals Prepared from Solution. *J. Am. Chem. Soc.* **2011**, *133*, 10679–10681. [CrossRef] [PubMed]
43. Liu, W.; Aguey-Zinsou, K.-F. Size effects and hydrogen storage properties of Mg nanoparticles synthesised by an electroless reduction method. *J. Mater. Chem. A* **2014**, *2*, 9718. [CrossRef]
44. Cornish-Bowden, A. Enthalpy-entropy compensation: A phantom phenomenon. *J. Biosci.* **2002**, *27*, 121–126. [CrossRef] [PubMed]
45. Zhao-Karger, Z.; Hu, J.; Roth, A.; Wang, D.; Kübel, C.; Lohstroh, W.; Fichtner, M. Altered thermodynamic and kinetic properties of MgH(2) infiltrated in microporous scaffold. *Chem. Commun. (Camb.)* **2010**, *46*, 8353–8355. [CrossRef] [PubMed]
46. Cuevas, F.; Korablov, D.; Latroche, M. Synthesis, structural and hydrogenation properties of Mg-rich MgH_2–TiH_2 nanocomposites prepared by reactive ball milling under hydrogen gas. *Phys. Chem. Chem. Phys.* **2012**, *14*, 1200. [CrossRef] [PubMed]
47. Lu, J.; Choi, Y.J.; Fang, Z.Z.; Sohn, H.Y.; Rönnebro, E. Hydrogen storage properties of nanosized MgH_2-0.1TiH_2 prepared by ultrahigh-energy-high-pressure milling. *J. Am. Chem. Soc.* **2009**, *131*, 15843–15852. [CrossRef] [PubMed]
48. Patelli, N.; Calizzi, M.; Migliori, A.; Morandi, V.; Pasquini, L. Hydrogen Desorption Below 150 °C in MgH_2–TiH_2 Composite Nanoparticles: Equilibrium and Kinetic Properties. *J. Phys. Chem. C* **2017**, *121*, 11166–11177. [CrossRef]
49. Mooij, L.P.A.; Baldi, A.; Boelsma, C.; Shen, K.; Wagemaker, M.; Pivak, Y.; Schreuders, H.; Griessen, R.; Dam, B. Interface energy controlled thermodynamics of nanoscale metal hydrides. *Adv. Energy Mater.* **2011**, *1*, 754–758. [CrossRef]
50. Patelli, N.; Calizzi, M.; Pasquini, L. Interface enthalpy-entropy competition in nanoscale metal hydrides. *Inorganics* **2018**, *6*, 13. [CrossRef]
51. Baldi, A.; Palmisano, V.; Gonzalez-Silveira, M.; Pivak, Y.; Slaman, M.; Schreuders, H.; Dam, B.; Griessen, R. Quasifree Mg-H thin films. *Appl. Phys. Lett.* **2009**, *95*, 20–22. [CrossRef]
52. Pivak, Y.; Schreuders, H.; Dam, B. Thermodynamic Properties, Hysteresis behavior and stress-strain analysis of MgH_2 thin films, studied over a wide temperature range. *Crystals* **2012**, *2*, 710–729. [CrossRef]
53. Kalisvaart, P.; Shalchi-Amirkhiz, B.; Zahiri, R.; Zahiri, B.; Tan, X.; Danaie, M.; Botton, G.; Mitlin, D. Thermodynamically destabilized hydride formation in "bulk" Mg–AlTi multilayers for hydrogen storage. *Phys. Chem. Chem. Phys.* **2013**, *15*, 16432–16436. [CrossRef] [PubMed]
54. Zhang, S.; Gross, A.F.; Van Atta, S.L.; Lopez, M.; Liu, P.; Ahn, C.C.; Vajo, J.J.; Jensen, C.M. The synthesis and hydrogen storage properties of a MgH(2) incorporated carbon aerogel scaffold. *Nanotechnology* **2009**, *20*, 204027. [CrossRef] [PubMed]
55. Nielsen, T.K.; Besenbacher, F.; Jensen, T.R. Nanoconfined hydrides for energy storage. *Nanoscale* **2011**, *3*, 2086–2098. [CrossRef] [PubMed]
56. Zlotea, C.; Oumellal, Y.; Hwang, S.-J.; Ghimbeu, C.M.; de Jongh, P.E.; Latroche, M. Ultrasmall MgH_2 nanoparticles embedded in an ordered microporous carbon exhibiting rapid hydrogen sorption kinetics. *J. Phys. Chem. C* **2015**, *119*, 18091–18098. [CrossRef]
57. De Jongh, P.E.; Allendorf, M.; Vajo, J.J.; Zlotea, C. Nanoconfined light metal hydrides for reversible hydrogen storage. *MRS Bull.* **2013**, *38*, 488–494. [CrossRef]
58. Xia, G.; Tan, Y.; Chen, X.; Sun, D.; Guo, Z.; Liu, H.; Ouyang, L.; Zhu, M.; Yu, X. Monodisperse magnesium hydride nanoparticles uniformly self-assembled on graphene. *Adv. Mater.* **2015**, *27*, 5981–5988. [CrossRef] [PubMed]
59. Jeon, K.-J.; Moon, H.R.; Ruminski, A.M.; Jiang, B.; Kisielowski, C.; Bardhan, R.; Urban, J.J. Air-stable magnesium nanocomposites provide rapid and high-capacity hydrogen storage without using heavy-metal catalysts. *Nat. Mater.* **2011**, *10*, 286–290. [CrossRef] [PubMed]

60. Asano, K.; Westerwaal, R.J.; Anastasopol, A.; Mooij, L.P.A.; Boelsma, C.; Ngene, P.; Schreuders, H.; Eijt, S.W.H.; Dam, B. Destabilization of Mg Hydride by Self-Organized Nanoclusters in the Immiscible Mg-Ti System. *J. Phys. Chem. C* **2015**, *119*, 12157–12164. [CrossRef]
61. Shegai, T.; Langhammer, C. Hydride formation in single palladium and magnesium nanoparticles studied by nanoplasmonic dark-field scattering spectroscopy. *Adv. Mater.* **2011**, *23*, 4409–4414. [CrossRef] [PubMed]
62. Syrenova, S.; Langhammer, C. Hydride formation thermodynamics and hysteresis in individual Pd nanocrystals with different size and shape. *Nat. Mater.* **2015**, *14*, 1236–1245. [CrossRef] [PubMed]
63. Makongo, J.P.A.; Prots, Y.; Burkhardt, U.; Niewa, R.; Kudla, C.; Kreiner, G. A case study of complex metallic alloy phases: Structure and disorder phenomena of Mg–Pd compounds. *Philos. Mag.* **2006**, *86*, 427–433. [CrossRef]
64. Huot, J.; Yonkeu, A.; Dufour, J. Rietveld analysis of neutron powder diffraction of Mg_6Pd alloy at various hydriding stages. *J. Alloys Compd.* **2009**, *475*, 168–172. [CrossRef]
65. Siviero, G.; Bello, V.; Mattei, G.; Mazzoldi, P.; Battaglin, G.; Bazzanella, N.; Checchetto, R.; Miotello, A. Structural evolution of Pd-capped Mg thin films under H_2 absorption and desorption cycles. *Int. J. Hydrog. Energy* **2009**, *34*, 4817–4826. [CrossRef]
66. Kelekar, R.; Giffard, H.; Kelly, S.T.; Clemens, B.M. Formation and dissociation of MgH_2 in epitaxial Mg thin films. *J. Appl. Phys.* **2007**, *101*, 1–7. [CrossRef]
67. Krozer, A.; Kasemo, B. Hydrogen uptake by Pd-coated Mg: Absorption-decomposition isotherms and uptake kinetics. *J. Less Common Met.* **1990**, *160*, 323–342. [CrossRef]
68. Chung, C.J.; Lee, S.C.; Groves, J.R.; Brower, E.N.; Sinclair, R.; Clemens, B.M. Interfacial alloy hydride destabilization in Mg/Pd thin films. *Phys. Rev. Lett.* **2012**, *108*, 1–4. [CrossRef] [PubMed]
69. Callini, E.; Pasquini, L.; Piscopiello, E.; Montone, A.; Antisari, M.V.; Bonetti, E. Hydrogen sorption in Pd-decorated Mg-MgO core-shell nanoparticles. *Appl. Phys. Lett.* **2009**, *94*. [CrossRef]
70. Callini, E.; Pasquini, L.; Rude, L.H.; Nielsen, T.K.; Jensen, T.R.; Bonetti, E. Hydrogen storage and phase transformations in Mg-Pd nanoparticles. *J. Appl. Phys.* **2010**, *108*. [CrossRef]
71. Pasquini, L.; Boscherini, F.; Callini, E.; Maurizio, C.; Pasquali, L.; Montecchi, M.; Bonetti, E. Local structure at interfaces between hydride-forming metals: A case study of Mg-Pd nanoparticles by X-ray spectroscopy. *Phys. Rev. B Condens. Matter Mater. Phys.* **2011**, *83*. [CrossRef]
72. Fernandez, J.F.; Ares, J.R.; Cuevas, F.; Bodega, J.; Leardini, F.; Sánchez, C. A thermodynamic study of the hydrogenation of the pseudo-binary $Mg_6Pd_{0.5}Ni_{0.5}$ intermetallic compound. *Intermetallics* **2010**, *18*, 233–241. [CrossRef]
73. Ponthieu, M.; Au, Y.S.; Provost, K.; Zlotea, C.; Leroy, E.; Fernández, J.F.; Latroche, M.; de Jongh, P.E.; Cuevas, F. Nanoconfinement of Mg_6Pd particles in porous carbon: Size effects on structural and hydrogenation properties. *J. Mater. Chem. A* **2014**, *2*, 18444–18453. [CrossRef]
74. Friedlmeier, G.; Arakawa, M.; Hirai, T.; Akiba, E. Preparation and structural, thermal and hydriding characteristics of melt-spun Mg–Ni alloys. *J. Alloys Compd.* **1999**, *292*, 107–117. [CrossRef]
75. Orimo, S.-I.; Fujii, H. Materials science of Mg-Ni-based new hydrides. *Appl. Phys. A* **2001**, *72*, 167–186. [CrossRef]
76. Zaluska, A.; Zaluski, L.; Ström-Olsen, J.O. Structure, catalysis and atomic reactions on the nano-scale: A systematic approach to metal hydrides for hydrogen storage. *Appl. Phys. A Mater. Sci. Process.* **2001**, *72*, 157–165. [CrossRef]
77. Montone, A.; Grbovic Novakovic, J.; Vittori Antisari, M.; Bassetti, A.; Bonetti, E.; Fiorini, A.L.; Pasquini, L.; Mirenghi, L.; Rotolo, P. Nano-micro MgH_2-Mg_2 NiH_4 composites: Tayloring a multichannel system with selected hydrogen sorption properties. *Int. J. Hydrog. Energy* **2007**, *32*. [CrossRef]
78. Callini, E.; Pasquini, L.; Jensen, T.R.; Bonetti, E. Hydrogen storage properties of Mg-Ni nanoparticles. *Int. J. Hydrog. Energy* **2013**, *38*. [CrossRef]
79. Gajdics, M.; Calizzi, M.; Pasquini, L.; Schafler, E.; Révész, A. Characterization of a nanocrystalline Mg-Ni alloy processed by high-pressure torsion during hydrogenation and dehydrogenation. *Int. J. Hydrog. Energy* **2016**, *41*, 9803–9809. [CrossRef]
80. Zou, J.; Sun, H.; Zeng, X.; Ji, G.; Ding, W. Preparation and Hydrogen Storage Properties of Mg-Rich Mg-Ni Ultrafine Particles. *J. Nanomater.* **2012**, *2012*, 1–8. [CrossRef]

81. Matsuda, J.; Yoshida, K.; Sasaki, Y.; Uchiyama, N.; Akiba, E. In situ observation on hydrogenation of Mg-Ni films using environmental transmission electron microscope with aberration correction. *Appl. Phys. Lett.* **2014**, *105*, 83903. [CrossRef]
82. Pasquini, L.; Callini, E.; Brighi, M.; Boscherini, F.; Montone, A.; Jensen, T.R.; Maurizio, C.; Antisari, M.V.; Bonetti, E. Magnesium nanoparticles with transition metal decoration for hydrogen storage. *J. Nanopart. Res.* **2011**, *13*. [CrossRef]
83. Bogerd, R.; Adelhelm, P.; Meeldijk, J.H.; de Jong, K.P.; de Jongh, P.E. The structural characterization and H_2 sorption properties of carbon-supported Mg_{1-x} Ni_x nanocrystallites. *Nanotechnology* **2009**, *20*, 204019. [CrossRef] [PubMed]
84. Zlotea, C.; Cuevas, F.; Andrieux, J.; Matei Ghimbeu, C.; Leroy, E.; Léonel, E.; Sengmany, S.; Vix-Guterl, C.; Gadiou, R.; Martens, T.; et al. Tunable synthesis of (Mg-Ni)-based hydrides nanoconfined in templated carbon studied by in situ synchrotron diffraction. *Nano Energy* **2013**, *2*, 12–20. [CrossRef]
85. Liang, G.; Schulz, R. Synthesis of Mg-Ti alloy by mechanical alloying. *J. Mater. Sci.* **2003**, *38*, 1179–1184. [CrossRef]
86. Asano, K.; Enoki, H.; Akiba, E. Synthesis of HCP, FCC and BCC structure alloys in the Mg-Ti binary system by means of ball milling. *J. Alloys Compd.* **2009**, *480*, 558–563. [CrossRef]
87. Borsa, D.M.; Gremaud, R.; Baldi, A.; Schreuders, H.; Rector, J.H.; Kooi, B.; Vermeulen, P.; Notten, P.H.L.; Dam, B.; Griessen, R. Structural, optical, and electrical properties of Mgy Ti1-y Hx thin films. *Phys. Rev. B Condens. Matter Mater. Phys.* **2007**, *75*, 1–9. [CrossRef]
88. Vermeulen, P.; Graat, P.C.J.; Wondergem, H.J.; Notten, P.H.L. Crystal structures of MgyTi100-y thin film alloys in the as-deposited and hydrogenated state. *Int. J. Hydrog. Energy* **2008**, *33*, 5646–5650. [CrossRef]
89. Calizzi, M.; Venturi, F.; Ponthieu, M.; Cuevas, F.; Morandi, V.; Perkisas, T.; Bals, S.; Pasquini, L. Gas-phase synthesis of Mg–Ti nanoparticles for solid-state hydrogen storage. *Phys. Chem. Chem. Phys.* **2016**, *18*, 141–148. [CrossRef] [PubMed]
90. Anastasopol, A.; Pfeiffer, T.V.; Middelkoop, J.; Lafont, U.; Canales-Perez, R.J.; Schmidt-Ott, A.; Mulder, F.M.; Eijt, S.W.H. Reduced enthalpy of metal hydride formation for Mg-Ti nanocomposites produced by spark discharge generation. *J. Am. Chem. Soc.* **2013**, *135*, 7891–7900. [CrossRef] [PubMed]
91. Vermeulen, P.; Niessen, R.A.H.; Notten, P.H.L. Hydrogen storage in metastable MgyTi(1−y) thin films. *Electrochem. Commun.* **2006**, *8*, 27–32. [CrossRef]
92. Baldi, A.; Gremaud, R.; Borsa, D.M.; Baldé, C.P.; van der Eerden, A.M.J.; Kruijtzer, G.L.; de Jongh, P.E.; Dam, B.; Griessen, R. Nanoscale composition modulations in MgyTi1-yHx thin film alloys for hydrogen storage. *Int. J. Hydrog. Energy* **2009**, *34*, 1450–1457. [CrossRef]
93. Ponthieu, M.; Cuevas, F.; Fernández, J.F.; Laversenne, L.; Porcher, F.; Latroche, M. Structural properties and reversible deuterium loading of MgD_2–TiD_2 nanocomposites. *J. Phys. Chem. C* **2013**, *117*, 18851–18862. [CrossRef]
94. Calizzi, M.; Chericoni, D.; Jepsen, L.H.; Jensen, T.R.; Pasquini, L. Mg-Ti nanoparticles with superior kinetics for hydrogen storage. *Int. J. Hydrog. Energy* **2015**. [CrossRef]
95. Krishnan, G.; Negrea, R.F.; Ghica, C.; ten Brink, G.H.; Kooi, B.J.; Palasantzas, G. Synthesis and exceptional thermal stability of Mg-based bimetallic nanoparticles during hydrogenation. *Nanoscale* **2014**, *6*, 11963–11970. [CrossRef] [PubMed]
96. Jangir, M.; Jain, A.; Agarwal, S.; Zhang, T.; Kumar, S.; Selvaraj, S.; Ichikawa, T.; Jain, I.P. The enhanced de/re-hydrogenation performance of MgH_2 with TiH_2 additive. *Int. J. Energy Res.* **2017**, 1–9. [CrossRef]
97. Shao, H.; Xin, G.; Zheng, J.; Li, X.; Akiba, E. Nanotechnology in Mg-based materials for hydrogen storage. *Nano Energy* **2012**, *1*, 590–601. [CrossRef]
98. Zhang, X.; Yang, R.; Qu, J.; Zhao, W.; Xie, L.; Tian, W.; Li, X. The synthesis and hydrogen storage properties of pure nanostructured Mg_2 FeH_6. *Nanotechnology* **2010**, *21*, 95706. [CrossRef] [PubMed]
99. Liu, W.; Setijadi, E.J.; Aguey-Zinsou, K.-F. Tuning the Thermodynamic properties of MgH_2 at the nanoscale via a catalyst or destabilizing element coating strategy. *J. Phys. Chem. C* **2014**. [CrossRef]
100. Bazzanella, N.; Checchetto, R.; Miotello, A.; Sada, C.; Mazzoldi, P.; Mengucci, P. Hydrogen kinetics in magnesium hydride: On different catalytic effects of niobium. *Appl. Phys. Lett.* **2006**, *89*, 5–7. [CrossRef]
101. Barkhordarian, G.; Klassen, T.; Bormann, R. Catalytic mechanism of transition-metal compounds on Mg hydrogen sorption reaction. *J. Phys. Chem. B* **2006**, *110*, 11020–11024. [CrossRef] [PubMed]

102. Tan, X.H.; Wang, L.Y.; Holt, C.M.B.; Zahiri, B.; Eikerling, M.H.; Mitlin, D. Body centered cubic magnesium niobium hydride with facile room temperature absorption and four weight percent reversible capacity. *Phys. Chem. Chem. Phys.* **2012**, *14*, 10904–10909. [CrossRef] [PubMed]
103. Schimmel, H.G.; Huot, J.; Chapon, L.C.; Tichelaar, F.D.; Mulder, F.M. Hydrogen cycling of niobium and vanadium catalyzed nanostructured magnesium. *J. Am. Chem. Soc.* **2005**, *127*, 14348–14354. [CrossRef] [PubMed]
104. Milošević, S.; Kurko, S.; Pasquini, L.; Matović, L.; Vujasin, R.; Novaković, N.; Novaković, J.G. Fast hydrogen sorption from MgH_2-VO_2(B) composite materials. *J. Power Sources* **2016**, *307*. [CrossRef]
105. Liang, G.; Huot, J.; Boily, S.; Van Neste, A.; Schulz, R. Hydrogen storage properties of the mechanically milled MgH2-V nanocomposite. *J. Alloys Compd.* **1999**, *291*, 295–299. [CrossRef]
106. Kyoi, D.; Sato, T.; Rönnebro, E.; Tsuji, Y.; Kitamura, N.; Ueda, A.; Ito, M.; Katsuyama, S.; Hara, S.; Noréus, D.; Sakai, T. A novel magnesium-vanadium hydride synthesized by a gigapascal-high-pressure technique. *J. Alloys Compd.* **2004**, *375*, 253–258. [CrossRef]